Title

Apparatus for Ultrahigh Precision Measurement of the 1S-2S Interval in Positronium

Author

Goldman, Harris J

Publication Date

2018

UNIVERSITY OF CALIFORNIA
RIVERSIDE

Apparatus for Ultrahigh Precision Measurement of $1^3S_1 - 2^3S_1$ Interval in Positronium

A Dissertation submitted in partial satisfaction
of the requirements for the degree of

Doctor of Philosophy

in

Physics

by

Harris J. Goldman

March 2018

Dissertation Committee:

Dr. Harry W. K. Tom, Chairperson
Dr. Allen P. Mills, Jr.
Dr. Hai-bo Yu

The Dissertation of Harris J. Goldman is approved:

Committee Chairperson

University of California, Riverside

Acknowledgments

This journey could not have been undertaken alone and there are many to acknowledge who have helped me get to this point.

Firstly, I must thank my advisor, Professor Harry Tom. His excitement and love for physics is contagious and is a constant source of energy. His insight and experience were invaluable to all aspects of the process of designing, constructing, and bringing the apparatus online. His intuition is truly remarkable. This project has been one of the highlights of my life and am so incredibly grateful to him to have had this opportunity.

None of this could have occurred without Professor Allen Mills, whose work over his entire career has pushed the field of positron and positronium physics to the point where this project could occur. His drive, expertise, and humor made everyday enjoyable.

Thanks to the guys in the machine shop: Mike Fournier, Jeff Lefler, and Daniel Adams. There was a tremendous amount of design and fabrication that went into this apparatus and I am grateful for their advice, instruction, creativity, and quality work. And also for the great conversation.

An important thank you must go to the staff here at UCR who truly make this place run. I want to specifically thank Ana Aldana, Erika Arzate, Derek Beving, Mayela Castillo, Jazmin Chavez, Sonia Godinez, and Jhon Gonzalez without whom none of this work could have been accomplished.

I want to thank Jack Reid for his help and tireless work throughout the years. I don't know what his exact job description is, but I'm certain he far exceeds it.

I have to thank Adrian and Donald who keep this place clean and provide necessary levity throughout my days.

Thank you to Rod Greaves and Jeremy Moxom for their important contributions to specifically designing, constructing, and designing parts of the positron and detection aspect of the apparatus. Their expertise and help is unsurpassed.

A special thank you to Adric Jones for not only the difficult job of proofreading this thesis, but for the collaboration during my time here. His productivity during my time here lifted all and I can't thank him enough for his tireless work.

I could not have made it without the support of my friends and family. It was not easy missing holidays and important occasions from across the country, but the calls, texts, and visits made it bearable. The support and love from everyone was and is overwhelming. A special thank you to my in-laws who feel like my #1 fans. And thank you to my parents for encouraging me to follow my dreams, even if they were 3000 miles away.

Finally, in many ways, I would not be here without the love, support, and patience of my wife, Ariela. Her ears and encouragement kept me going and her doubt in my biased perspective kept me optimistic. Truly, the entire project and collaboration is indebted to her demand that there must be an end in sight! I Love You.

To science, the search for truth, and fact-based reasoning in these strange times.

ABSTRACT OF THE DISSERTATION

Apparatus for Ultrahigh Precision Measurement of $1^3S_1 - 2^3S_1$ Interval in Positronium

by

Harris J. Goldman

Doctor of Philosophy, Graduate Program in Physics
University of California, Riverside, March 2018
Dr. Harry W. K. Tom, Chairperson

Positronium (Ps) is a purely leptonic atom comprising an electron and its antimatter equivalent, the positron, in a quasi-stable bound state. Due to its fundamental nature, Ps is an ideal test bed for bound-state QED.

Recent high-precision spectroscopic experiments reveal a discrepancy in the measurement of the proton charge radius r_p, known as the Proton Charge Radius Puzzle. Spectroscopic measurments carried out on hydrogen and muonic hydrogen, the bound state of a muon and a proton, differ from other scattering and other spectroscopic experiments by 3.3σ. The measurement of r_p comes from fitting the resulting measurement of either the 1S-2S interval of hydrogen or the Lamb Shift in muonic hydrogen to theory.

Neither of these atoms are governed purely by quantum electrodynamics (QED) alone as nuclear structure has a role to play. The ratio of the masses of the orbiting particle m to that of the nucleus M is a coefficient in a number of a QED corrections to the energy levels of hydrogen ($m/M = 1/1836$) and muonic hydrogen ($m/M = 207/1836$) and reveals

the importance of performing a complementary spectroscopic measurement in Ps, where $m/M = 1$.

The last measurement of the 1S-2S interval was carried out by Fee, Mills, Chu, et al. in 1993 to a precision of 3.2 ppb. The state-of-the-art measurement on hydrogen is now at an uncertainty of 4.2×10^{-15}. While the simplicity of Ps causes it to be appealing to test bound-state QED, its antiparticle-particle nature makes it difficult to work with: the ground state lifetime of the triplet state is 142 ns, and whereas the 2S lifetime in Ps is 1.14 μs, the 2S lifetime in hydrogen is 105× longer.

We have designed and constructed an apparatus and experiment to measure the 1S-2S interval in Ps at precision levels that we expect to immediately improve upon the previous measurements by factor of 2× and pave the way for ultimate comparison to the hydrogenic measurements. The apparatus also opens the doors to a new frontier in high-precision spectroscopy: the sub-μs regime.

Contents

List of Figures

List of Tables

Chapter 1

Introduction

1.1 Positronium

Positronium (Ps) is a hydrogen-like atom that comprises the quasi-stable bound state of an electron (e^-) and its anti-matter counterpart the anti-electron, also known as a positron (e^+). Observation of the positron was first reported by Anderson [1], only four years after it was first theorized by Dirac in 1928 [2, 3]. The existence of positronium was theorized to exist just two years later (1934) by Mohorovičić [4] and it was first observed in experiments 17 years later by Deutsch [5]. Another 31 years would pass before spectroscopic excitation was demonstrated by Chu and Mills in 1982 [6].

Due to its simplicity and similarity to hydrogen, positronium is of great interest to the fundamental physics community. Many of its properties can be calculated using the non-relativistic Schrödinger equation by substituting in the reduced mass of positronium

$$\mu_{Ps} = \frac{m_{e^+} m_{e^-}}{m_{e^+} + m_{e^-}} = \frac{m_{e^-}}{2} \tag{1.1}$$

From this simple substitution, we can calculate many of the important hydrogenic properties to at least first order. The Bohr radius is simply twice that of hydrogen, $a_{Ps} = 2a_0$, and the binding energy of the ground state is just half that of hydrogen

$$\frac{1}{2}E_1(H) = -6.3 \text{ eV} \tag{1.2}$$

We can take many of the tools that we've acquired working typical textbook problems with hydrogen and immediately apply them to positronium.

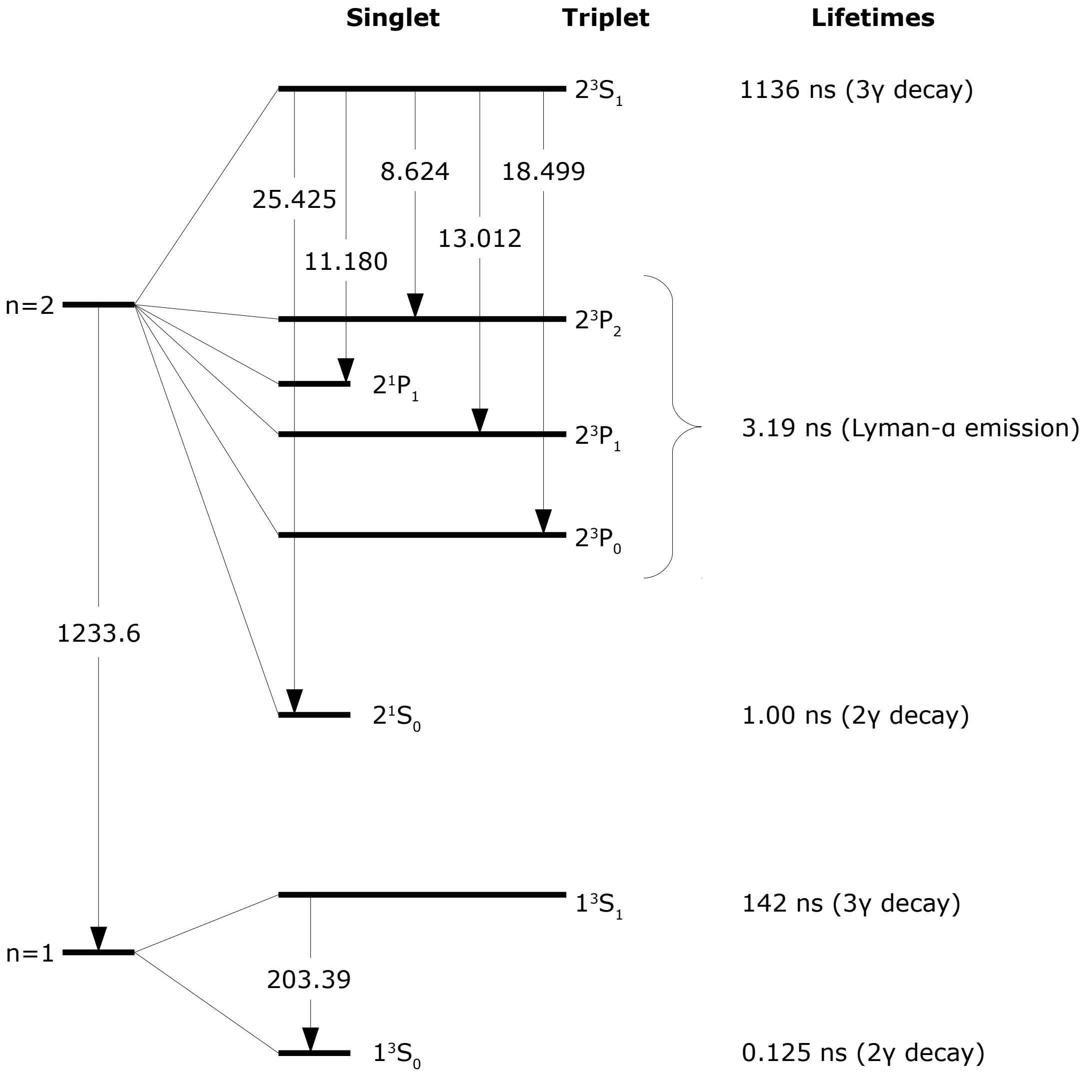

Figure 1.1: Energy level diagram for positronium with intervals given in units of GHz along with state lifetimes.

However, unlike hydrogen, positronium's existence is short-lived. Since it is composed of equal parts matter and anti-matter, and due to its symmetric nature, Ps can annihilate whereby its mass-energy is converted into electromagnetic gamma-ray (γ) radiation. The singlet and triplet ground states exist for 0.125 ns and 142 ns primarily decaying into either 2γ with energy of 511 keV each and 3γ of total energy 1022 keV, respectively.

Annihilation also occurs in the higher atomic states, and defines the lifetimes of the 2S states; however for states 2P and above, the atomic lifetime is dominated by the radiative decay rate to lower states where annihilation again dominates. The lifetimes and energy spacings of the first and second excited states are shown in Fig. 1.1 [7, 8]. Positronium's ephemeral nature and the fact that it partly comprises antimatter mean that it is difficult to generate in large quantities.

Positronium's simplicity is owed to the fact that it contains no hadronic particles but comprises only leptons, elementary particles that do not experience the strong or weak nuclear force. This property makes Ps an ideal testbed for bound-state quantum electrodynamics (QED). Bound-state QED is the theory of the interaction between light and matter, specifically photons and charged leptons, in bound systems. QED was a leap forward in physics with its first success being the explanation for Lamb's observation that the $2S_{1/2}$ and $2P_{1/2}$ states in hydrogen are not degenerate as predicted by the Dirac equation [9].

Due to the symmetric nature of Ps, other interesting and particularly complicating properties arise. Because of the electron's and positron's opposite charge and equal mass [10], Ps has no net magnetic moment. Ps becomes unwieldy in its higher order QED calculation corrections, since the atom is composed of a matter-antimatter pairing, annihilation terms must be considered. However, its symmetry also means it is the most sensitive to higher order corrections because the mass ratio is unity, meaning it is 2000× more sensitive to these corrections than hydrogen.

Theoretical calculations of the Ps energy levels are presently at the sub-kHz level. The terms in the expansion of the energy carry a coefficient of $R_\infty \alpha^n \log^p \alpha$ where $R_\infty =$

$\alpha^2 mc/h$ is the Rydberg constant with m the electron mass, c the speed of light, and h the Planck constant; α is the fine structure constant; and n, p are integers. The "fine-structure" correction was calculated by Ferrell [11]. Contributions due to self-energy and vacuum polarization as well as recoil and retardation were added by Fulton and Martin [12], but were only valid for the n=2 state. Fulton later generalized to n=1 [13]; however Gupta et al. [14] derived a general equation using a different method that reproduced the original Fulton and Martin results, but slightly differed from Fulton's later result for n=1. Fell provided the correction at $R_\infty \alpha^4 \ln\alpha$ [15]. Pachucki and Karshenboim then pushed forward and summarized the corrections for $R_\infty \alpha^4$ [16] and provided a correction at the $R_\infty \alpha^5 \ln^2\alpha$ level [17]. The latest correction was carried out by Adkins et al. at the level of $R_\infty \alpha^5$ [18].

The corrections are presented below in their general form as much as possible:

$$\frac{E_0}{h} = -\frac{1}{2n^2}c(R_\infty) \tag{1.3}$$

$$\frac{E_1}{h} = 2\frac{1}{n^3}c(R_\infty \alpha^2)\left[\frac{11}{64}\frac{1}{n} + \frac{1}{12}\right] \tag{1.4}$$

$$\frac{E_2}{h} = -\frac{6}{4\pi}\frac{1}{n^3}c(R_\infty \alpha^3 \mathrm{ln}\alpha) \tag{1.5}$$

$$\begin{aligned}\frac{E_3}{h} &= \frac{1}{4\pi}\frac{1}{n^3}c(R_\infty \alpha^3) \\ &\times \left\{\frac{14}{3}\left[\frac{7}{15} + \ln(2/n) + \frac{n-1}{2n} + \sum_{k=1}^{n}\frac{1}{k} + \mathrm{ln}2\right] - \frac{16}{3}\mathrm{ln}R(n,0) - 4\left(\frac{16}{9} + \mathrm{ln}2\right)\right\}\end{aligned} \tag{1.6}$$

$$\frac{E_4}{h} = -\frac{1}{6}\frac{1}{n^3}c(R_\infty \alpha^4 \mathrm{ln}\alpha) \tag{1.7}$$

$$\frac{E_5}{h} = \begin{cases} 2c(R_\infty \alpha^4)\left[0.16107(63) + 0.3925(17) \times \frac{1}{4}\right], & n = 1 \\ \frac{1}{4}c(R_\infty \alpha^4)\left[0.34557(63) - 0.1048(17) \times \frac{1}{4}\right], & n = 2 \end{cases} \tag{1.8}$$

$$\frac{E_6}{h} = -\frac{2}{\pi}\frac{1}{n^3}c(R_\infty \alpha^5 \mathrm{ln}^2\alpha)\left(\frac{499}{480} + \frac{7}{32}\right) \tag{1.9}$$

In Table 1.1, the result of each correction and the final overall correction is shown. The constants used to derive the values were $\alpha^{-1} = 137.035999160$, $R_\infty = 10973731.568508$ from the 2014 CODATA [19], with the Bethe logarithms given as $R(1,0) = 2.9841285$ and $R(2,0) = 2.8117699$.

The Fee et al. result of 1233607216.4 ± 3.2 MHz differs from theory by $\sim 1.8\sigma$ with theory nearing the kHz level of contribution [20].

Table 1.1: QED corrections to the 1^3S_1 and 2^3S_1 levels and the $1^3S_1 - 2^3S_1$ interval in MHz.

Order	$\Delta\nu(1^3S_1)$	$\Delta\nu(2^3S_1)$	$\Delta\nu(2^3S_1 - 1^3S_1)$
R_∞	-1644920980.18	-411230245.04	1233690735.13
$R_\infty\alpha^2$	89419.20	7413.58	-82005.62
$R_\infty\alpha^3\ln\alpha + R_\infty\alpha^3$	1733.14	231.71	-1501.43
$R_\infty\alpha^4\ln\alpha$	7.65	0.96	-6.69
$R_\infty\alpha^4$	1.17	0.75	-0.42
$R_\infty\alpha^5\ln^2\alpha$	-1.32	-0.17	1.16
$R_\infty\alpha^5$			-0.01
Total	-1644829819.02	-411222598.05	1233607222.11

1.2 Proton Charge Radius Puzzle

The necessity for a new higher-precision measurement of the 1S-2S interval of positronium is evident based purely on the level of precision that theory has achieved, behind which experiment lags. An improved measurement at the sub-MHz level will push theorists to tackle the increasingly complex higher order correction terms and determine if theory and experiment are converging. However, the interest does not end in purely chasing ever greater precision for its own sake.

The so-called Proton Charge Radius Puzzle is a disagreement between results for the charge radius of the proton (r_p), which is a necessary variable in the description of the energy levels in hydrogenic atoms with a proton-containing nucleus. Until recently, the results from electron-proton scattering, hydrogen spectroscopy [21], and microwave experiments [22] were in agreement, but in disagreement with the spectroscopic experiment on muonic-hydrogen (μp), the bound state of a proton and muon [23]. The discrepancy in proton charge radius described from spectroscopy of H and μp discepancy was 4.5σ and almost 7σ if scattering data was included. The hydrogen group has published new results suggesting a correction to the Rydberg constant and a new value of r_p that is within 1σ of the μp result, but now 3.3σ from the mean of previous H measurements and CODATA 2014 values [24].

The μp measurement is much more sensitive to r_p due to the heavier muon having greater overlap with the nuclear wavefunction and an m/M coefficient an order of magnitude larger than in H, which allows direct comparison with the hydrogen experiments even with a less precise measurement.

Since the μp results were published, groups have been revisiting the electron-proton scattering data. The new analyses vary in their results from bringing all measurements into alignment [25] to maintaining the discrepancy between the spectroscopy experiments and scattering experiments [26, 27]. Further, more precise, experiments are still warranted.

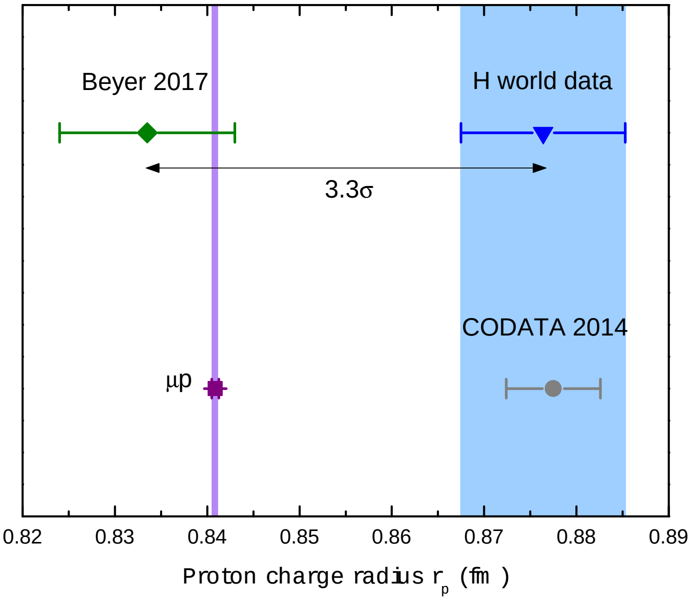

Figure 1.2: Proton charge radius results from various experiments reproduced from Beyer et al [24].

Positronium's simplicity is what makes it an ideal test of the bound-state QED terms alone: there are no added variables due to the presence of a hadronic nucleus and the mass ratio of unity means it is the most sensitive to higher-order corrections. While QED has been incredibly successful at explaining the observations of atoms like H and μp, due to the presence of a hadron, there may be some physics obscured that is preventing universal agreement in r_p. Questions obviously remain: is there an underlying error to either the spectroscopy or scattering experiments? does the addition of r_p need to be reformulated? do the currently accepted values of some of the physical constants, e.g. R_∞, need to be adjusted? is there some unaccounted for physical phenomena required in the QED calculations? An improvement in the measurement of the 1S-2S interval of Ps to the kHz level will enable a direct comparison to the H and μp QED terms and either confirm them or perhaps reveal a surprise.

Chapter 2

Experimental Apparatus

2.1 Positronium Apparatus

2.1.1 Source stage

Our experiments use a ^{22}Na source that produces positrons via β^+ decay, whereby a proton becomes a neutron releasing a positron, electron neutrino, and a 1.27 MeV gamma ray.

$$ {}^{22}_{11}\mathrm{Na} \rightarrow {}^{22}_{10}\mathrm{Ne} + e^+ + \nu_e + \gamma(1.27 \text{ MeV}) \tag{2.1} $$

and thus the ^{22}Na becomes stable ^{22}Ne. The source has a half-life of 2.6 years and the current activity level is ∼5 mCi. The positrons are emitted with energies up to ∼500 keV; in order to produce usable positrons, their energy spread and maximum must be greatly reduced through a process known as moderation. Our apparatus employs a solid neon moderator [28] whereby neon gas is frozen at ∼7 K on the inside surface of a conical opening immediately in front of the positron source [29]. About 1% of the positrons emitted from the source are subsequently re-emitted from the moderator with a 1-3 eV energy spread and a mean energy defined by a repulsive potential applied to the moderator. The cold, moderated positrons are then separated from the hot, unmoderated positrons by a velocity selector. A magnetic saddle coil deflects the slow positrons through an off-axis aperture in a tungsten plug, and a second saddle coil is used to steer the beam back onto the axis of the guiding solenoids. The fast unmoderated positrons are not significantly deflected by the magnetic fields and are thus lost to annihilation in the source assembly, tungsten plug, and the walls of the source stage vacuum chamber.

The positrons are then guided electrostatically to the trap stage. All of this occurs under vacuum (10^{-9} Torr) and in the presence of magnetic fields produced by coils around the apparatus. These conditions are necessary to prevent usable positrons from interacting with matter and annihilating.

2.1.2 Trap stage

The moderated positrons are accumulated in a Surko-type buffer gas trap [30–33], as shown in Fig. 2.1, to create bunches of positrons that can be released at variable repetition rates. The lower limit to the repetition rate is based upon diminishing trap efficiency, where the ($1/e$ filling time is typically on the order of 1 s) and the upper limit is dependent upon either the minimum time for data collection or a reduced signal rate. It is typically operated at a rate of ~1-2 Hz. The trap serves the purpose of reducing the energy spread, and the thus the phase space, of the positrons, while also confining and accumulating a large number of them ($\sim 2 \times 10^5$/s). A large solenoid surrounds the trap in order to create a uniform axial magnetic field that constrains the positrons radially as each positron is bound in cyclotron motion about an axis defined by the magnetic field line.

Positrons from the dc moderated beam are trapped primarily by inelastic collisions with N_2 buffer gas [34]. At 10 eV, positrons excite a vibronic transition (a combination of electronic and vibrational excitation) in the N_2, losing 8-9 eV i the process. After three such collisions, the positrons are in the deepest part of the potential well, known as stage 3, where the buffer gas pressure is lowest. In this stage, repeated collisions with the SF_6 and N_2 thermalize the trapped positrons to the temperature of the gas.

Although these collisions allow the positrons to be energetically confined within the potential well, they have the effect of shifting the cyclotron axis. Many such collisions thus lead to an expansion of the trapped cloud. To counteract this, one of the two electrodes defining stage 3 is segmented. A rotating bias potential is applied to this electrode, cycling at $\sim$5 MHz [35,36]. The rotating electric field, known as a 'rotating wall', compresses the positron cloud toward the axis, greatly increasing the storage lifetime and the density of the positron beam produced. The rf field pumps some heat into the stored positron cloud, however this is rapidly dissipated by the SF_6 buffer gas [37].

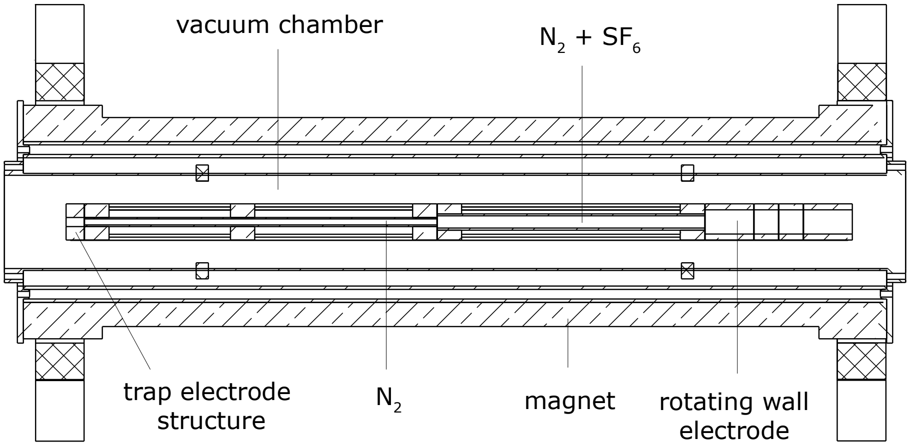

Figure 2.1: Schematic of the trap stage of the positron apparatus.

While it is necessary to have relatively high pressures in the trap to maximize the trapping efficiency, high pressure is undesirable elsewhere. The gas pressure directly outside of the trap is minimized by introducing N_2 directly into the first stage, which has a small internal diameter and thus a low conductance rate. The trap stage is isolated from the adjacent source stage and pulsed transport stages via differential pumping; narrow constrictions are installed that reduce the pressure by a factor of $\sim 10^3$ in both directions.

The positron apparatus from the source stage to the trap stage is shown in Fig. 2.2.

2.1.3 Target stage

The positrons are dumped out of the trap by shorting the gate potential to ground producing pulses of $\sim 10^5$ e^+s about 30 ns wide. Positrons enter a pulsed accelerator ~ 1 μs later. The accelerator serves two main purposes: the first is to provide a tunable positron energy to ensure proper thermalization by varying the implantation depth profile; the second

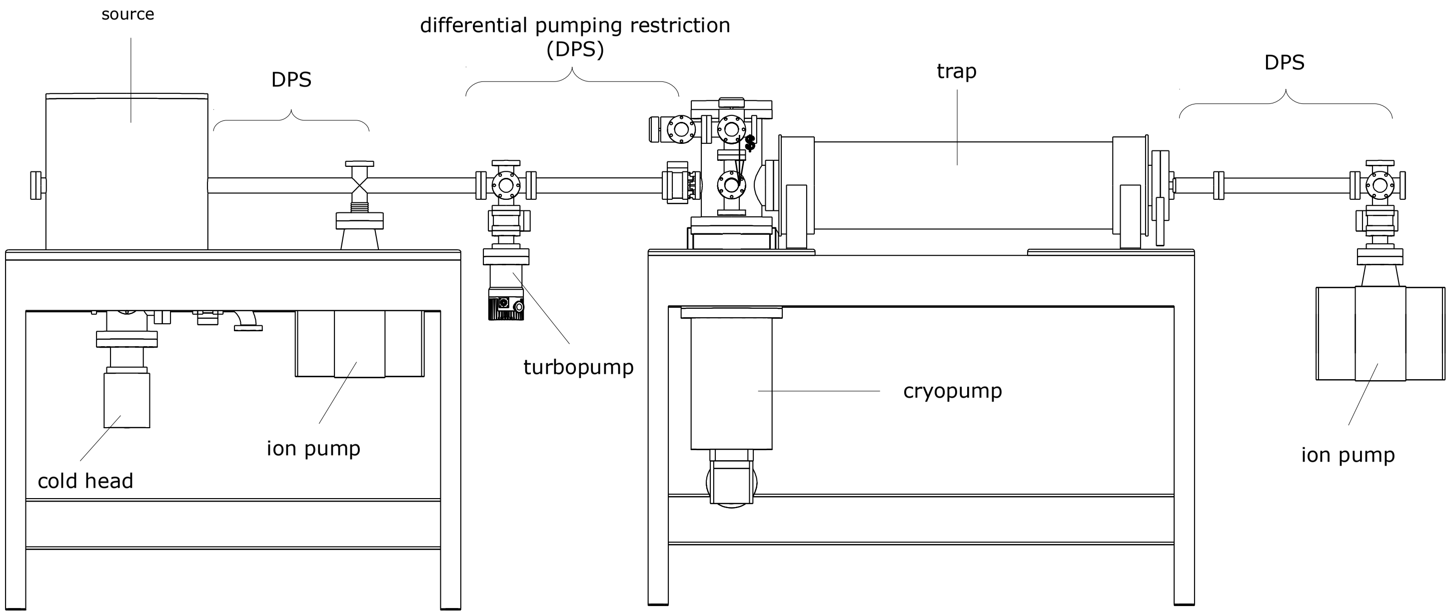

Figure 2.2: The source and trap stages of the positron beamline, specifically illustrating the vacuum systems involved.

is to bunch the positrons and accelerate them with minimal energy spread, ensuring optimal performance from the subsequent electrostatic lens. The first third of the accelerator is wired to produce a parabolic potential, such that positrons are bunched prior to acceleration. The remaining two thirds of the accelerator form a linear ramp, providing a smooth adiabatic acceleration of the pulses. The accelerator produces bunches of positrons with mean energies of ≤ 5 keV, an energy spread of ~ 200 V FWHM, and a temporal spread of ~ 10 ns FWHM.

Immediately after the accelerator, positrons are extracted from the confining magnetic field through a 3 mm aperture in a μ-metal shield. The shield serves to rapidly terminate as much of the magnetic field, allowing the 1S-2S measurement to be conducted in a region that is very nearly field-free.

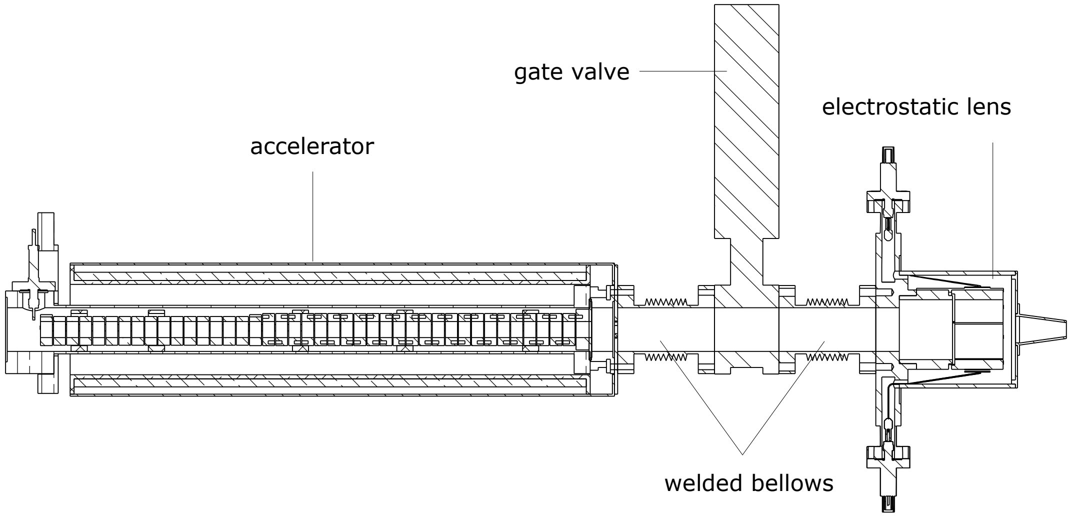

Figure 2.3: Schematic of the accelerator and electrostatic lens stages of the positron apparatus.

After transport through two vibration-isolating bellows, the expanding beam of positrons then encounters the electrostatic focusing lens, an Einzel lens system with a segmented electrode providing a means of precisely steering the focused beam at the target.

A narrow spatial distribution is vital to reduce the positional uncertainty of the Ps emitted for calculating any effects pertaining to the trajectory of the atom. The electrostatic lens means that we avoid any more magnetic fields, which are detrimental due to the speeds of emitted Ps and the motional Stark shift, discussed below. Unfortunately, residual dc electric fields are also undesirable as they result in shifts as well. This influence has been mitigated by not only the standoff distance of the lens from the interaction region, but also by the addition of a grounded, conical snout, which greatly attenuates the electric field of the lens at the target and in the region of excitation. The lens focuses positron pulses to a 100-300 μm FWHM spot at the target.

Positron interactions with solid surfaces have been studied extensively [38, 39]. When slow positrons are implanted in an appropriate target (e.g. single-crystal metals such as Cu, Al), they are known to form Ps relatively efficiently, dependent upon implantation energy and target temperature [40,41]. Formation typically produces thermal or epithermal Ps [42], although nearly monoenergetic Ps has been observed [43]. Ps may not be formed at all and positrons that do not annihilate in the target can be re-emitted with low energies [44]. Thermal Ps is produced when positrons that have been thermalized in the bulk become trapped in the image potential well at the target's surface. At high enough temperatures, these positrons are able to escape the well due to thermal fluctuations, grabbing an electron to become Ps in the process [45,46]. Alternatively, epithermal Ps is produced from positrons that have not fully thermalized in the target and escape at energies greater than the ground-state Ps work function [47] allowing for the production of excited-state Ps [48] or from spontaneous emission, where the energy of the Ps emitted is dominated by the momentum of the electron.

The ultimate goal is to use a single-crystal Al(111) target prepared such that a sub-monolayer of oxygen resides on its surface. This preparation has been shown to produce a significant amount of thermal Ps at target temperatures below 300 K [49]. Difficulties arise due to the strong dependence upon target surface contamination, amount of oxygen present, and intense laser beams near the surface. Initial experiments will be carried out with porous silica, which produces thermal Ps at room temperature, but has the effect of broadening the time distribution of emission [50].

2.1.4 Ps Count rate

We consider the Ps emitted from the target in a beam Maxwellian distribution [51], which is applicable in the case of an atom emitted from a hole with a diameter much smaller than its mean free path. The distribution takes the form of $\upsilon_z f(\upsilon)$ where υ_z are velocities normal to the sample and $f(\upsilon)$ is the Maxwell-Boltzmann distribution:

$$\upsilon_z f(\upsilon) = \tilde{A}\upsilon_z e^{-m\upsilon^2/2k_\mathrm{B}T} d^3\vec{\upsilon} \tag{2.2}$$

where $\tilde{A}$ is the normalization constant, m is the mass of the atom, k_B is the Boltzmann constant and T is the temperature.

The physical situation lends itself to using cylindrical coordinates where $d^3\vec{\upsilon} = 2\pi\upsilon_\rho d\upsilon_\rho \upsilon_z d\upsilon_z$ and υ_ρ is the cylindrical-radial velocity.

$$dn(\vec{\upsilon}) = N\left(\frac{m}{k_{\mathrm{B}}T}\right)^2 e^{-m\upsilon_\rho^2/2k_{\mathrm{B}}T}\upsilon_\rho d\upsilon_\rho e^{-m\upsilon_z^2/2k_{\mathrm{B}}T}\upsilon_z d\upsilon_z \tag{2.3}$$

where $\tilde{A} = \frac{N}{2\pi}\left(\frac{m}{k_{\mathrm{B}}T}\right)^2$ and N is the total number of atoms. By using the relation $\upsilon_\rho^2 = \upsilon_z^2 \tan^2\theta$ and $\tan^2\theta \ll 1$,

$$dn(\upsilon_z, \alpha \leq \theta \leq \beta) \approx \frac{1}{2}N\left(\frac{m}{k_{\mathrm{B}}T}\right)^2 (\tan^2\beta - \tan^2\alpha)e^{-m\upsilon^2/2k_{\mathrm{B}}T}\upsilon^3 d\upsilon_z \tag{2.4}$$

where α, β is the angular range within which atoms will encounter our detector. The exponential term is ≈ 1 such that

$$dn(\upsilon_z, \alpha \leq \theta \leq \beta) \approx \frac{1}{2}N\left(\frac{m}{k_{\mathrm{B}}T}\right)^2 (\tan^2\beta - \tan^2\alpha)\upsilon_z^3 d\upsilon_z \tag{2.5}$$

Integrating from $\upsilon = 0$ to $\upsilon_{z,\max}$ produces

$$n(\upsilon_z \leq \upsilon_{z,\max}, \alpha, \beta) = \frac{8N}{\pi^2}(\tan^2\beta - \tan^2\alpha)\left(\frac{\upsilon_{z,\max}}{\bar{\upsilon}}\right)^4 \tag{2.6}$$

with $\bar{\upsilon} = \sqrt{8k_{\mathrm{B}}T/\pi m}$.

There are a couple of things worth noting here. The count rate scales as $\upsilon_{z,\max}^4$. Since the lineshape of the 1S-2S interval is shifted and broadened as a function of speed (see Sec. 2.3), we are most interested in the slowest moving atoms. For two velocity groups that differ by a factor of 2, the number of counts expected is 16× different. The count rate also scales as $\vec{v}^{-4}$, which is proportional to T^{-2}. This indicates that, for thermal Ps, if we can lower the sample from 300 K to 100 K, we will increase the counts n by a factor of 9.

For each pulse from the trap, we have $\sim 10^5$ e^+. Using a silica target, as will be the case for our preliminary experiments, we have $\sim 30\%$ vacuum Ps production [52] per implanted positron, 3/4 of which is emitted as triplet Ps. Assuming the detector collects with equal efficiency over its entire active area, which relies on complete spatial and temporal coverage of the outgoing Ps with the laser, then the detector represents a fractional coverage of $\sim 0.7\%$, though due to the extreme angle, the effective collection will likely be approximately halved as a result of the angular distribution of Ps emission from the target. As such, if we could saturate the transition, i.e. 100% excitation to the Rydberg levels, then we would expect ~ 80 counts/shot. The temporal overlap of the Rydberg excitation laser with the outgoing Ps beam, which we expect to be ~ 20 ns FWHM is far below unity, as its pulse duration is ~ 5 ns FWHM. As such, this would reduce the anticipated count rate by a factor of 3-4 at best. Furthermore, even with sufficient power to saturate the transition, only half of the Ps atoms leaving each laser would be in the excited state - a total factor of 12×, bringing the expected count rate to perhaps 5 counts/shot. In practice, due to the dependence of excitation on the intensity squared, as well as a desire to minimize the ac Stark shift, we expect much less than this.

2.1.5 Rydberg Positronium

The largest shift to the resonance frequency of the Ps will be the second-order Doppler shift, which is on order of tens of MHz. This effect is unavoidable until we can trap Ps so we must correct the data, which is limited by the uncertainty in our measurement of an atom's speed. The 2S lifetime is on order of 1μs and an atom moving at 10^5 m/s will only travel 10 cm in that time. If this distance is known to 1 mm and the time is known to 1 ns, there would be an uncertainty in this shift around 1.5 MHz. If the atoms could survive long enough to travel 3× farther, the uncertainty is down to 500 kHz. Since the uncertainty in determining the mean of a population is limited by the sample size, if we want to get our uncertainty to the 100 kHz level, it would take ~10× less time if we are able to detect our atoms at a 30 cm distance. The limit then is the lifetime of the Ps atom, which we can readily extend by exciting Ps from the 2S state to Rydberg states of $n \geq 25$ where the velocity uncertainty is only limited by the size of our chamber and the distance away that we can place the detector.

A Rydberg state is an electronically excited state with a high principal quantum number. We have successfully carried out experiments exciting and detecting Ps in a two-step process from the triplet ground state to the first excited state (2P) with a 243 nm photon and then to Rydberg states of nD or nS, where $n = 15 - 30$, with a ~ 732 nm photon [53, 54]. The light used for excitation in these experiments was produced from two pulsed dye lasers (Quanta Ray PDL-1) pumped by the second and third harmonic light generated by a pulsed Continuum Surelite III Nd:YAG laser. The 243 nm light was produced from the second harmonic of tunable 486 nm light generated by one dye laser running with LD489 dye dissolved in methanol; the tunable 732 nm light was created from LDS 751 also dissolved in methanol in the other dye laser.

When an atom is excited to a Rydberg state it is highly sensitive to electric fields because the increased distance between the positron and the electron creates a large electric dipole moment. With the atom so polarized the orbits are no longer circular and the Schrödinger equation is more readily solved using a parabolic coordinate system. The result of this is that the usual angular momentum quantum number l is replaced with new parabolic quantum numbers n_1 and n_2 [55].

In the majority of our experiments, we use metal targets that are grounded with no insulators nearby such that there are no static electric fields due to charging. However, without specific effort used to combat the issue, a non-zero magnetic field could be present as magnets are used to guide positrons through the source and trap stages and keep away from the chamber walls and Earth's field, without shielding or cancellation, contributes $\sim$0.5 Gauss field at the target. This leads to an induced electric field $\vec{F} = \vec{v} \times \vec{B}$. To first order, this produces a motional Stark shift of [56]

$$\Delta E_{\text{Stark}} = \frac{3}{2} n k e a_{0_{Ps}} |\vec{F}| \tag{2.7}$$

where $k = n_1 - n_2$ has values in the set $\{-(n - |m| - 1) : 2 : +(n - |m| - 1)\}$, $\vec{F}$ is the electric field, and $a_{0\text{Ps}}$ is twice the Bohr radius. An atom in the first excited state with a velocity of 10^5 m/s perpendicular to a modest field of 10 G will experience an $\sim$8 MHz shift.

In Rydberg states, the lifetime of the atom is dominated by radiative decay processes and not by annihilation [57, 58]. Radiative decay can occur in one step to a ground state or via any number of allowed optical transitions to lower states and ultimately annihilation. The lifetime of Rydberg Ps atoms has been recently studied by Deller et al. [59] with respect to the available parameters n, m, and k. They calculate that the gross fluorescence lifetime with respect to n scales as n^4, while within a specific level the fluorescence lifetime is essentially constant for $|m| = 1, 2$ but for $|m| = 0$ the lifetime varies greatly from high-$|k|$ to low-$|k|$ states. They find that for $n = 20$, the mean lifetime is $\sim 25 \pm 5$ μs, thus at 30 cm from the target for Ps with $v = 10^5$ m/s $< 15\%$ would be expected to decay.

2.2 High finesse optical cavities and stabilization

Before we get into the details of the spectroscopy and metrology of the experiment, we will review the important terms and facets of working with high finesse optical cavities.

2.2.1 Properties of optical cavities

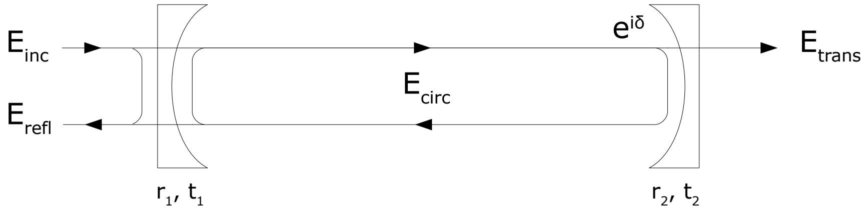

Figure 2.4: Schematic of electric fields pertaining to an optical resonator.

An optical cavity is a device in which light can be stored. Our experiment only utilizes cavities consisting of two mirrors, but this is not the only possible design. The electric fields incident E_{inc}, reflected E_{refl}, circulating E_{circ}, and transmitted E_{trans} from a cavity comprising two mirrors with electric-field transmission and reflection coefficients of t_i and r_i separated by length L are shown in schematic form in Fig. 2.4 and are related by [60]:

$$E_{\mathrm{circ}} = \frac{t_1}{1 - r_1 r_2 e^{2i\delta}} E_{\mathrm{inc}} \tag{2.8}$$

$$E_{\mathrm{trans}} = t_2 E_{\mathrm{circ}} = \frac{t_1 t_2 e^{i\delta}}{1 - r_1 r_2 e^{2i\delta}} E_{\mathrm{inc}} \tag{2.9}$$

$$E_{\mathrm{refl}} = r_1 E_{\mathrm{inc}} - r_2 t_1 e^{2i\delta} E_{\mathrm{circ}} = \left(r_1 - \frac{t_1^2 r_2 e^{2i\delta}}{1 - r_1 r_2 e^{2i\delta}} \right) E_{\mathrm{inc}} \tag{2.10}$$

where $\delta = 2\omega n L/c$ is the phase shift for half a round trip with $f = \omega/2\pi$ the frequency of the light, n is the index of refraction of the medium, and c the speed of light in vacuum. This can be rewritten as $\delta = \omega/\Delta\nu_{\mathrm{FSR}}$ with the introduction of the free spectral range $\Delta\nu_{\mathrm{FSR}} = c/2nL$.

The transmission from such a cavity has the shape of an Airy function with

$$I_{\mathrm{trans}} = |E_{\mathrm{trans}}|^2 = I_{\mathrm{inc}} \frac{T_1 T_2}{(1 - \sqrt{R_1 R_2})^2 + 4\sqrt{R_1 R_2} \sin^2(\delta)} \tag{2.11}$$

where $T_i = t_i^2$ and $R_i = r_i^2$ are the intensity transmission and reflection coefficients of the mirrors. The linewidth of a cavity $\delta\nu_{\mathrm{FWHM}}$ is a function of what is known as the finesse $\mathcal{F} = \Delta\nu_{\mathrm{FSR}}/\delta\nu$; these properties are illustrated in Fig. 2.5. The finesse of an optical resonator is defined by the internal losses, which for a cavity in vacuum are due to mirror quality [60]:

$$\mathcal{F} = \frac{2\pi}{\mathcal{L}} \tag{2.12}$$

where $\mathcal{L}$ is the total round trip loss contributed to transmission (T_i), scatter (S_i), and absorption (A_i) for each mirror, such that $\mathcal{L} = \sum_{i=1}^{2} T_i + S_i + A_i$.

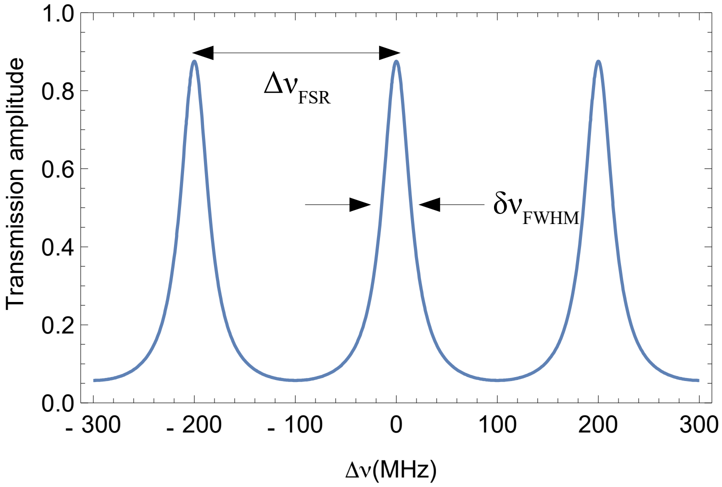

Figure 2.5: Transmission from a lossy optical cavity with a free spectral range of 200 MHz.

For light that stays resonant with a cavity, the only light transmitted is that which is coupled to the transmitted mode; for imperfect mode-matching, the other light is wasted. The power transmitted can be written in terms of the useful incident light ϵP_{inc} where ϵ explicitly includes loss due to mode matching.

$$\frac{P_{\text{trans}}}{\epsilon P_{\text{inc}}} = \frac{4T_1T_2}{\mathcal{L}^2} = 4T_1T_2\left(\frac{\mathcal{F}}{2\pi}\right)^2 \tag{2.13}$$

The circulating power can be expressed similarly

$$\frac{P_{\text{circ}}}{\epsilon P_{\text{inc}}} = \frac{4T_1}{\mathcal{L}^2} = 4T_1\left(\frac{\mathcal{F}}{2\pi}\right)^2 \tag{2.14}$$

By combining equations 2.14 and 2.13, we can ultimately derive an equation to determine the important parameter of circulating power as a function of the transmitted power

$$P_{\text{circ}} = \frac{P_{\text{trans}}}{T_2} \tag{2.15}$$

It is useful to determine the major source of loss in the cavity, which helps in ascertaining the best way to improve finesse. Following the work of Hood et al. [61] we can derive a way through measuring the incident, reflected, and transmitted powers to separate out the loss due to transmission and scatter/absorption. The useful reflected power is written as

$$\frac{P_{\text{refl}} - (1-\epsilon)P_{\text{inc}}}{\epsilon P_{\text{inc}}} = \frac{(T_2 + l_1 + l_2 - T_1)^2}{\mathcal{L}^2} = (l_1 + l_2 + T_2 - T_1)^2 \left(\frac{\mathcal{F}}{2\pi}\right)^2 \tag{2.16}$$

where $l_i = S_i + A_i$. We can write down the relationship between the transmitted and reflected powers as

$$\frac{P_{\text{trans}}}{P_{\text{refl}} - P_{\text{inc}}} = \frac{4T_1T_2\left(\frac{\mathcal{F}}{2\pi}\right)^2}{(l_1 + l_2 + T_2 - T_1)^2\left(\frac{\mathcal{F}}{2\pi}\right)^2 - 1} \tag{2.17}$$

and if we assume that mirrors from the same coating run have the same transmission loss such that $T_1 = T_2$, we can solve for the loss due to transmission and scatter/absorption using equations 2.12 and 2.17.

2.2.2 Pound-Drever-Hall method of locking

We will now describe the Pound-Drever-Hall (PDH) method of locking here as it is vital to our experiment; it is a commonly used technique and has been discussed extensively [62–65]. The following explication follows Black closely [63].

When a laser's frequency can be continuously adjusted to stay on resonance with a cavity, the cavity and laser are said to be locked together. There are different methods to lock to a cavity, of which the most popular is the PDH technique. A laser that is incident upon an optical cavity will transmit light only within the linewidth about the resonance of that cavity. Any light that is not on resonance will be reflected; when the laser is locked to the cavity, the circulating light that leaks out back towards the incident light will destructively interfere with the reflected light from the front face sending the reflection signal towards zero. The reflected signal thus provides useful information about the difference in frequency between the laser and cavity resonance.

One could try to use just the bare reflected signal to keep on resonance; however, two problems arise: (1) the reflection signal is symmetric such that you cannot lock to the peak of the intensity, but rather the side; and (2) you cannot differentiate between intensity changes due to frequency detuning and those due to amplitude modulation on the laser itself. The PDH method produces an antisymmetric error signal that is monotonic across the resonance such that when the zero-crossing is set to coincide with resonant frequency, one can reliably lock to the center frequency of the cavity.

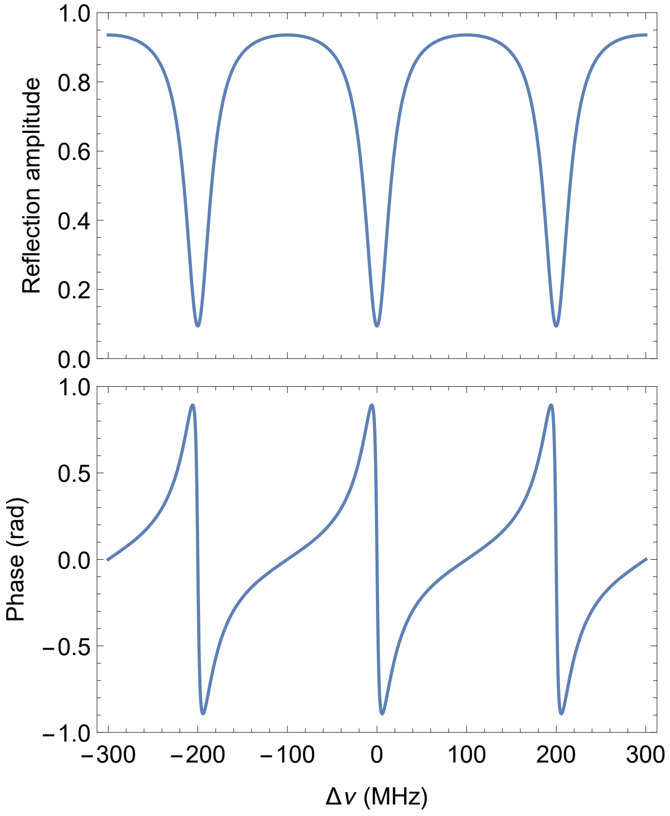

Figure 2.6: The reflected signal and electric-field phase from a lossy optical cavity.

To derive the PDH error signal, the laser is phase modulated, in our experiment with electro-optic modulators (EOM)

$$E_{\text{inc}} = E_0 e^{-i(\omega + \beta \sin \Omega t)} \tag{2.18}$$

where ω is the carrier frequency, Ω is the modulation frequency, and β is the modulation depth. The effect of phase modulation results in a main carrier at the center frequency and sidebands on either side of the carrier at $\omega \pm \Omega$. The phase modulation is always set to be much larger than the cavity linewidth so that near resonance, the sidebands are fully reflected. A photoreceiver observing the reflected signal from the cavity will detect the beating of the different frequencies involved producing signals at dc, Ω, and 2Ω. It is the coefficients of the Ω term that contain the important information and so the signal is mixed with the local oscillator frequency that produces the sidebands and then a low-pass filter is employed to pull out the error signal, as derived in detail below.

The incident field can be written as an infinite series using Bessel functions

$$E_{\text{inc}} = E_0 J_0(\beta) e^{-i\omega t} + \sum_{k=1}^{\infty} J_k(\beta)\left(e^{-ik\Omega t} + (-1)^k e^{ik\Omega t}\right) E_0 e^{-i\omega t} \tag{2.19}$$

which explicitly shows how the sidebands appear. For a modest modulation depth, the higher-order sidebands will be negligible such that we will focus on the first-order sidebands on either side of the carrier.

The reflected signal picked up by a photodetector will as usual be proportional to the square magnitude of the electric field ($P \propto \frac{1}{2}|E|^2$)

$$P_{\text{refl}} = \frac{1}{2}|E_c + E_s e^{-i\Omega t} - E_s e^{i\Omega t}|^2 \tag{2.20}$$

$$= P_c|F(\omega)|^2 + P_s\{|F(\omega+\Omega)|^2 + |F(\omega-\Omega)|^2\} \tag{2.21}$$

$$+ 2\sqrt{P_c P_s}\{\Re[F(\omega)F(\omega+\Omega)^* - F(\omega)^* F(\omega-\Omega)]\cos\Omega t$$

$$+ \Im[F(\omega)F(\omega+\Omega)^* - F(\omega)^* F(\omega-\Omega)]\sin\Omega t\} + \mathcal{O}(2\Omega)$$

where the subscript c denotes a carrier term, subscript s denotes a sideband term, and F is the reflection coefficient $E_{\text{refl}}/E_{\text{inc}}$, which is a function of the field's frequency. Since Ω is large enough such that the sidebands will always be reflected, $F(\omega \pm \Omega) \approx 1$ and therefore

$$F(\omega)F(\omega+\Omega)^* - F(\omega)^*F(\omega-\Omega) \approx i2\Im[F(\omega)] \tag{2.22}$$

is purely imaginary and the $\cos \Omega t$ term is zero. This signal from the photodiode is then mixed with the oscillator supplying the modulation

$$\sin(\Omega t)\sin(\Omega' t) = \cos(\Omega - \Omega')t - \cos(\Omega + \Omega')t \tag{2.23}$$

Thus for $\Omega = \Omega'$ and with a low-pass filter we would pass the dc term. In practice there will always be at least a nominal phase shift between the local oscillator and the signal, such that a phase shifter is used to correctly align the signals to produce the best result.

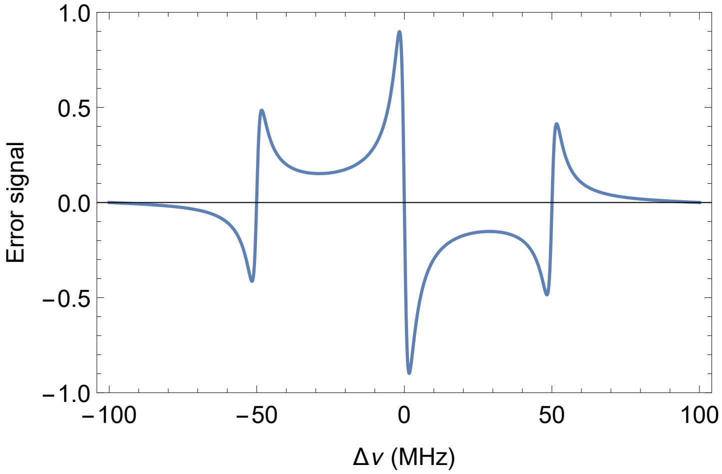

Figure 2.7: A Pound-Drever-Hall (PDH) error signal produced from imparting sidebands at ± 50 MHz on a laser.

The expected shape of an error signal as a laser is swept across resonance is shown in Fig. 2.7 for a modulation frequency of $\Omega = 50$ MHz. It is evident that around the cavity's resonance, the error signal is anti-symmetric, monotonic, linear, and can be set to cross at any point based upon a chosen dc offset. For no offset, the zero crossing will coincide with the center of the resonance and any deviation can be understood and corrected to drive the error signal back to zero.

2.3 Excitation

The accuracy to which a measurement of an energy interval in atom can be made is related to the linewidth of that transition. The linewidth is primarily determined by the effects of homogeneous and inhomogeneous broadening [66]. In the homogeneous case, the atoms are indistinguishable such that all of their energy transitions are the same, but the width is due to various factors that decrease the atomic coherence time and affect all of the atoms equally. Inhomogeneous broadening is the case where the atoms are distinguishable and the spectral width is affected by the individual resonant transitions of the atoms, an example of which is the velocity distribution of atoms in a gaseous state. A transition between the 1S and 2S states of an atom produces a narrow linewidth.

The 1S-2S interval is specifically chosen because of the relatively long 1.136 μs lifetime of the 2S state. The linewidth of the 1S-2S transition is characterized by a sum of all of the processes that contribute to the dephasing of the coherent field-atom interaction:

$$\frac{1}{T} = \sum_i \frac{1}{\tau_i} = \frac{1}{0.142\ \mu\mathrm{s}} + \frac{1}{8 \times 0.142\ \mu\mathrm{s}} \tag{2.24}$$

which results in a lifetime of 126.2 ns. This means that the natural linewidth of the 1S-2S transition is

$$\delta\nu = \frac{1}{2\pi}\frac{1}{T} = 1.261\ \mathrm{MHz} \tag{2.25}$$

which is very narrow compared to the linewidths of other levels in Ps with shorter lifetimes. These properties are owed to the fact that the transition from levels of the same parity is dipole-forbidden and therefore the lifetime of the 2S state is dominated by the rate of annihilation.

Fortunately, we can excite to a transition between states of the same parity with two-photon absorption [67]. Even more beneficial is that a two-photon excitation from counter-propagating beams of the same frequency produces a first-order Doppler-free result. When a moving atom is excited by two-photon absorption, the photon it is traveling towards will be blue-shifted and the photon it is traveling away from will be red-shifted. Since both photons have the same frequencies, these opposite shifts will have the same magnitude. Therefore, no matter the velocity of the atom, in its rest frame, the sum of the frequencies will always be the same. The consequence of this is that when the laser is tuned to be near the frequency of the atomic transition, every atom within the beam will be excited.

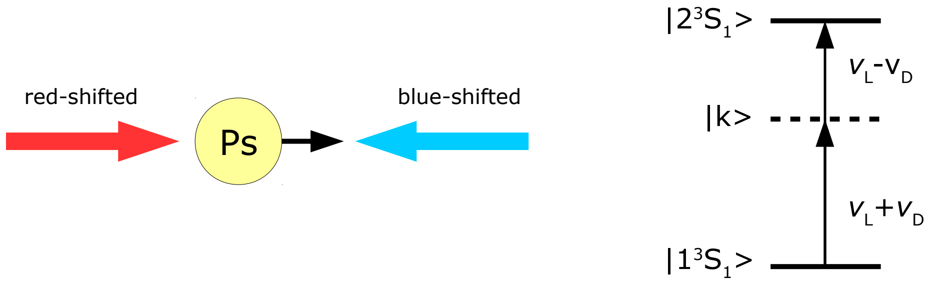

Figure 2.8: The first-order Doppler free excitation of an atom illustrated. On the left, two photons that come from the same source will be shifted in frequency equal and oppositely from the perspective of the atom. On the right, the shifted frequencies will always sum to the full interval frequency.

Two-photon absorption can be described as a two-step process whereby the atom is excited from an initial state $|i\rangle$ to a final state $|f\rangle$ via an intermediate virtual state $|k\rangle$. The virtual state is a sum of all of the possible real states that can connect $|i\rangle$ to $|f\rangle$ via allowed single-photon transitions [68].

The design of the excitation cavity was chosen specifically to try to reduce perturbation effects and improve upon the results of Fee et al. [20]. A natural consequence of the single-frequency, two-photon excitation using counter-propagating beams is that the transition will be free of the first-order Doppler shift. As such, the primary shifts and sources of broadening in our experiments are the: (1) dc Stark shift; (2) ac Stark shift; (3) motional Stark shift; (4) second-order Doppler shift; and (5) transit-time broadening. Additionally, we are concerned with creating a stable environment for our sensitive cavity which means reducing as much as possible sources of electronic, acoustic, thermal, and vibrational noise in a terribly noisy lab.

The Stark shifts are minimized as much as possible by design, with residual shifts directly calculable for each detected atom and readily subtracted from the final result. A dc Stark shift will arise if any charging of the apparatus takes place. For example, our cavity is supported by four glass rods. Electrons created from photoionization by our cw laser or unconverted, re-emitted positrons from the target could cause the rods to charge up. To prevent this, we have painted the faces of the rods that will see charged particles with silver paint and grounded the paint to our stainless steel (SS) supports.

In initial experiments we are using a pressed silica (SiO_2) sample; SiO_2 has been shown to produce thermal positronium [69] with 40% efficiency for an implantation energy of 1.5 keV [52]. Unfortunately silica is an insulator and can also accrue charge that will create a static field directly at the excitation region. In future experiments, we intend to use single crystal Al(111), treated with a sub-monolayer coating of oxygen [49]. This is the only metal target that has been demonstrated to produce thermal Ps at room temperature or colder and will be less likely to support a significant surface charge.

The ac Stark shift is an unavoidable effect of the presence of the laser light. It is given by:

$$\Delta\nu_{\text{Stark}} = 13.3\ \frac{\text{cm}^2}{\text{J}} \times I(\vec{r})\ \frac{\text{W}}{\text{cm}^2} \tag{2.26}$$

for the full 1S-2S interval. Its effect is directly measurable by changing the light intensity and extrapolating the measured interval to find the field-free value. Additionally, we will have position sensitive detection, discussed in Sec. 2.4.4, that will allow us to know the trajectory of the atom through the laser and thus the intensity of the field traversed. Furthermore, our cavity geometry, discussed below, means that we will have a fairly large beam diameter at the excitation region, which yields a lower peak intensity than that of a smaller beam, such as that used in the experiments of Fee et al. [20]

The motional Stark shift due to any residual magnetic fields is also a problem. The apparatus has been designed to be non-magnetic by avoiding magnetic materials and degaussing any magnetized parts when possible. The axial magnetic fields used to guide the positrons through the source and trap stages are terminated well before the target and the positrons are accelerated through a mu-metal aperture to further reduce any residual fields. The earth's magnetic field, $\leq 47\ \mu\text{T}$ around our apparatus, will provide a ~ 360 kHz shift if not nulled.

The second-order Doppler shift $\delta\nu_D$ for the full 1S-2S interval is given by:

$$\begin{aligned} \delta\nu_D(v) &= -\frac{1}{2}\left(\frac{v}{c}\right)^2 \nu_0(1^3S_1 - 2^3S_1) \\ &= -1.234 \times 10^9 \frac{1}{2}\left(\frac{v}{c}\right)^2 \ \text{MHz} \end{aligned} \tag{2.27}$$

This effect is much more pronounced in Ps spectroscopy than other atomic species due to the absence of a heavy nucleus. A Ps atom with the same kinetic energy as an hydrogen atom will be moving $\sim 30\times$ faster and thus have a second-order Doppler shift $\sim 900\times$ greater. For example, thermal Ps atoms from a room temperature source have a mean speed of 10^5 m/s, resulting in a shift of around -70 MHz.

Our design allows us to know accurately the shifts engendered by the various effects as we will have recorded the four-dimensional position of each particle detected. With this knowledge, we can back out each atom's trajectory and determine the magnitudes of the various shifts it experiences. Furthermore, we can down-select our data to consider only the slowest moving atoms that will have the smallest influence from the various effects.

Transit-time broadening can be thought of as a manifestation of the Heisenberg uncertainty principle: the shorter (longer) the interaction time between the atom and the field, the broader (narrower) the energy level of the excited state appears. The transit-time broadening $\Delta\nu_{tt}$ due to the finite time τ_{tt} the atom spends in the beam is given by [70]:

$$\Delta\nu_{tt} = \frac{1}{2\pi}\left[0.5346/\tau_{\text{nat}} + \sqrt{0.2166/\tau_{\text{nat}}^2 + 22.18/\tau_{tt}^2}\,\right] \tag{2.28}$$

where τ_{nat} is the natural lifetime of the state. It is evident from Eqn. 2.28 that as $\tau_{tt} \to \infty$, $\Delta\nu_{tt}$ approaches the natural linewidth.

In order to reduce the magnitude of this effect by increasing τ_{tt}, we made two choices in the geometry of the apparatus relating to the detection of Ps.

Firstly, the position of our MCP detector is oblique to the interaction region. This means that detected atoms will travel some distance $2\omega/cos\theta$ sideways in the beam where ω is the beam radius at that position and θ will vary with each atom depending on where they hit the position sensitive detector with $\theta = 0$ corresponding to an atom emitted normal from the surface of the target. The angle to the center of our detector $\sim$30 cm away is $\theta \approx 84^\circ$.

Secondly, our optical cavity geometry was chosen to create a fat beam at the interaction region. The $\sim$70 cm long cavity buttressed by concave mirrors of 50 cm and 20 cm means that the beam diameter 2ω in the interaction region, about 10 cm from the 50 cm mirror, is $\sim$1.7 mm.

Therefore, with these implementations, for atoms moving at 10^5 m/s and hitting the center of the detector, the expected transit-time broadening is $\sim$5 MHz. If the atoms were traveling straight through the beam, the expected broadening would be more than 8× greater. For the geometry of Fee et al, the transit-time broadening was $\sim$50 MHz.

2.4 Spectroscopy Apparatus

2.4.1 Overview

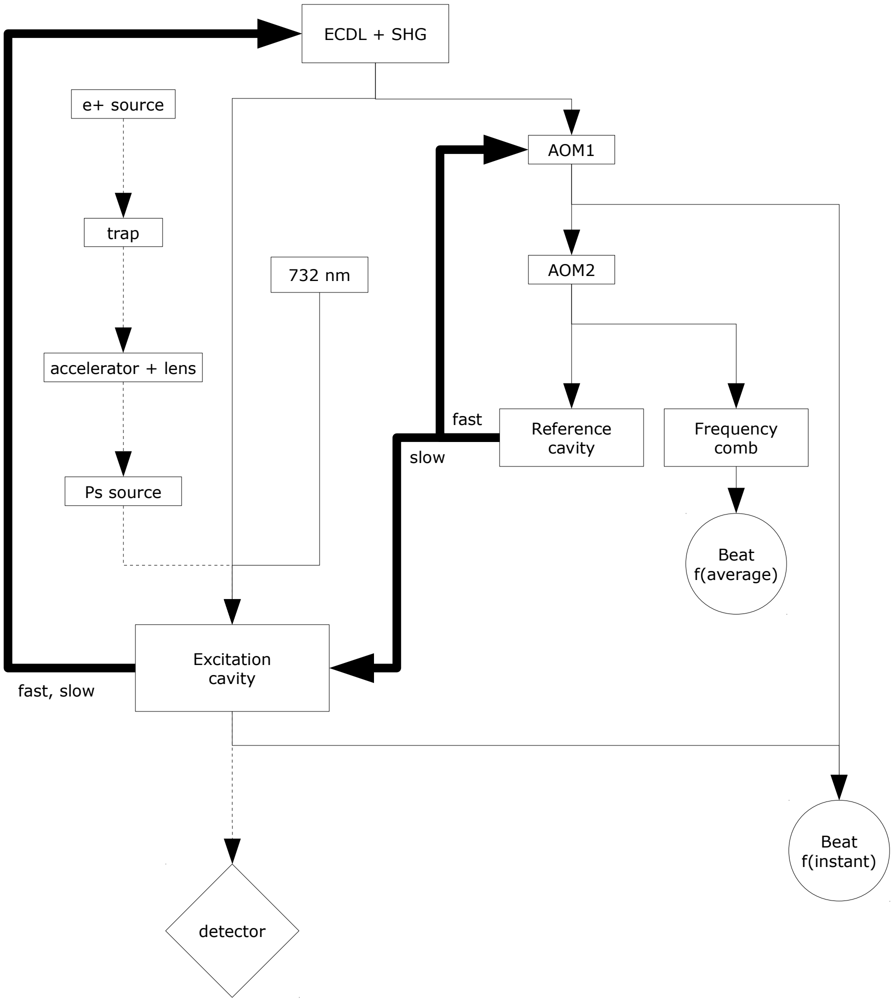

Figure 2.9: Schematic overview of the experimental apparatus. The thin solid lines indicate optical beam; thick solid lines indicate feedback as related to PDH cavity locking; the dashed lines indicate particle (e^+/Ps) flow. The slow (fast) refers to the < 1 Hz (> 1 Hz) feedback bandwidth for maintaining lock.

Our apparatus is designed to push ultrahigh precision spectroscopy into the sub-μs timescales. The excitation of the atom from the ground state to the first excited state must take place within the 142 ns lifetime of the ground state. By utilizing an ultrastable reference cavity to measure our average frequency over periods $> 100\times$ longer, limited only by how long we remain at a fixed frequency as we scan across resonance, we take full advantage of the supreme accuracy of our frequency comb. Therefore, the instantaneous frequency of the atomic excitation in the very short time window is able to read as an offset to the average frequency measured by the comb.

The following is an overview of the spectroscopic components to the experiment and how they are linked together. The laser is locked to the main excitation cavity using the Pound-Drever-Hall method (PDH) where the error signal is derived using an electro-optic modulator (EOM). The fast branch is fed back to the source laser and is introduced as a dc modulation on the laser current to track and correct against high frequency noise (> 1 Hz). The slow feedback is provided to a piezoelectric transducer (piezo, pzt) on a grating in the fundamental cavity to track and correct against large, slow drifts (< 1 Hz). Simultaneously, we lock to the ultra-stable reference cavity via an acousto-optic modulator (AOM1). The fast part of the error signal derived from this cavity is fed back to AOM1, which nullifies noise up to 200 kHz. The slow feedback is sent to the piezo of the excitation cavity to provide frequency tuning capability. We scan the frequency by using a second AOM (AOM2) on the reference cavity breadboard.

The light that has been stripped of high frequency noise after double-passing AOM1 is picked off and beat against the exit light of the main excitation cavity. This provides an instantaneous frequency offset between the stable reference cavity and the noisy main cavity at the time of atomic excitation. The light that has traversed both AOMs and is locked to the reference cavity is picked off and sent to the frequency comb and provides an average frequency measurement. This design allows us to reap the most out of the comb by beating the comb line against a very stable reference.

This will produce a value for the 1S-2S interval through the following relations:

$$\langle f_{\text{laser}} \rangle = f_{\text{comb}} - 2f_{\text{AOM2}} - 2f_{\text{AOM1}} \tag{2.29}$$

$$\delta f_{\text{laser}} = f_{\text{beat}} - 2f_{\text{AOM1}} \tag{2.30}$$

$$f_{\text{1S-2S}} = 2(\langle f_{\text{laser}} \rangle + \delta f_{\text{laser}}) \tag{2.31}$$

where $\langle f_{\text{laser}} \rangle$ is the average frequency measured via the reference cavity, δf_{laser} is the instantaneous frequency, f_{beat} is the frequency produced from beating the light after AOM1 with the light exiting the excitation cavity, f_{comb} is the result of the comb measurement, and the AOM values are doubled because each one is used in a double-pass configuration.

2.4.2 Laser

The source laser used to excite the Ps was purchased from Toptica Photonics, Inc. An extended cavity diode laser (ECDL) at 972 nm passes through a tapered amplifier and then to a second-harmonic generating (SHG) cavity where up to 1 W of continuous-wave (cw) 486 nm light is generated. About 85% of the light (> 800 mW) is sent directly to the excitation cavity. The rest is sent by fiber to our metrology table and then further split and routed to our reference cavity, frequency comb, atomic reference, and various diagnostics.

The entire laser box is milled from a single, solid block of aluminum, known as a hog-out, a process which ensures the final product is high-tolerance and free of stress that may result from casting or an assembly of imperfectly fitted components, thus guaranteeing maximal stability. The ECDL has been demonstrated to produce a free-running linewidth of < 10 kHz in 5μs. The SHG cavity is locked to the fundamental using the PDH technique with phase modulation provided by an external EOM, as an alternative to current modulation, in order to obviate detrimental intensity and frequency modulation. The lock is carried out using two pzts: a small, fast response pzt to cancel out high frequency noise and a larger pzt for nullifying larger, slower drifts.

We send the photodiode signal to the Toptica PDD110 where it can be amplified and is then mixed with the same rf supplied to the EOM and phase adjusted to produce the optimum error signal. The error signal is then fed into a Toptica Fast Analog Linewidth Control (FALC) 110 where the modulation frequency is blocked with a low-pass filter and the gain and feedback of the correction signal is fine-tuned to achieve the best balance of gain to bandwidth for tightest locking.

The correction signal is split into two branches to decouple the fast response from the slow. The fast response is fed to the fast-response pzt to provide high speed correction; the slow branch is fed to the larger, slow-response pzt to correct larger, slower drifts such as that due to temperature change. The SHG cavity only has a finesse of $\sim$300 so the lock is fairly easy and robust.

The main output of the cw laser is also locked to the main excitation cavity. The positron beamline is a noisy apparatus in all aspects and needed significant upgrades to stabilize the apparatus mechanically for use in a high-precision optical spectroscopy experiment. We have undertaken substantial effort to reduce the noise level of the apparatus, and to better isolate the remaining noise; however, the operation of the trap and cryogenic source moderator necessitates the use of relatively loud, high-speed pumps. Furthermore, due to the complexity of operation of these stages, and the fact that the beamline is used for multiple experiments, there are many substantial persistent and transient sources of electrical noise. Due to these circumstances, we have opted to lock the laser to the main excitation cavity, taking advantage of its high-bandwidth response, as opposed to locking the cavity to the laser in a similar fashion to the SHG locking.

The laser is locked to the main excitation cavity in the same manner that the SHG cavity is locked: an error signal is derived using the PDH method and the PDD 110 and FALC 110 modules. Phase modulation is generated by an external EOM (Qubig EO-F45K3-VIS) that is temperature controlled to reduce the effects of residual amplitude modulation. The main difference from the SHG lock is that both the fast and slow feedback are supplied to the master oscillator: the fast feedback is provided to the dc modulation input on the laser current and the slow feedback is provided to a pzt in the master oscillator cavity.

A portion of the main output of the cw laser is picked off and sent via optical fiber (Evanescent Optics, Inc. Corning PM48-U25D) to a separate optical table containing our metrology components. Each optical table is housed in its own separate temperature-controlled enclosure. The metrology setup is thus almost fully decoupled from the noisy

UHV apparatus. From this table, light is sent via fiber to the reference cavity breadboard, an atomic reference breadboard, and various other diagnostics like power and beam-position monitors.

2.4.3 Optical cavity

Due to our cavity geometry, its extreme sensitivity, and the noisiness of the positron beamline, we put a fair amount of effort into designing and engineering solutions to dampen and isolate vibration as much as possible. The entire UHV apparatus, shown in Figs. 2.11 and 2.12, is sitting upon a $6' \times 4' \times 18''$ optical table with a resonance frequency of ~ 100 Hz. The table sits upon legs capable of holding loads up to 2000 lbs each with a vertical resonance at ~ 1 Hz and 94% isolation at 5 Hz. The main chamber and pumps are built upon an isolation table floating on our main optical table. This isolation table is constructed of non-magnetic SS, primarily consisting of $3'' \times 2'' \times 1/4''$ tubing. The isolation table is floated on compact air mounts (Newport SLM-6A) that have a resonance of < 5 Hz and $> 95\%$ isolation at 10 Hz. Every large accessible flange is clamped with a yoke and connected to either the isolation table or the floor. The idea is to increase the resonance frequency of the system as a whole to well above the resonance of the optical table. The chamber's only connections to the optical table are through the SLM-6As and bellows that are below the chamber. The bellows allow us to connect the optical cavity directly to the table while allowing the chamber to independently move and vibrate. The bellows that are around the upright supports are illustrated in Fig. 2.10.

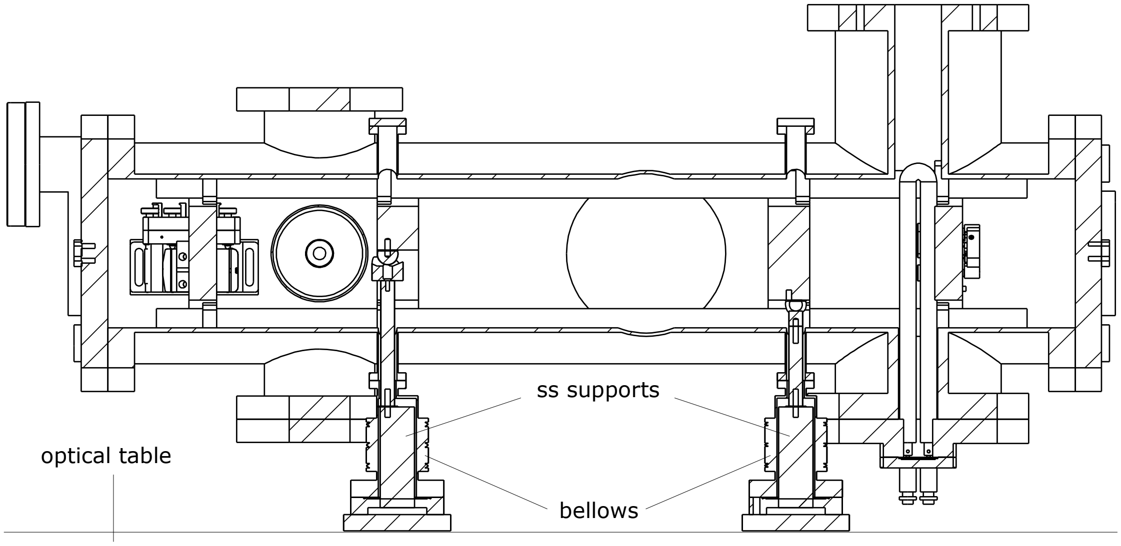

Figure 2.10: A drawing of the optical cavity inside the UHV chamber showing how the cavity is connected to the optical table and the chamber is floated.

The UHV apparatus is large and tall, which created an inverted pendulum when the optical table was floated. In order to combat this, we lowered the center of mass by adding a SS box filled with lead beneath the table.

The particularly complex design of the apparatus is due to a couple of reasons. During operation, the cavity is extremely sensitive to vibration such that we must use mechanically quiet ion pumps. However, because our detector is sensitive to ions, there cannot be a direct line of sight between the detector and an ion pump. Due to this necessary standoff, we've used large diameter nipples to maintain high conductance, but have also added an additional high speed pump to make up for the reduced pumping speed. We've also planned for future experiments that will attempt to make use of an Al target, which requires special preparation, by adding a secondary chamber into which the target can be retracted with a manipulator and isolated from the main chamber. The sample-prep chamber was designed to be able to carry out Ar ion sputtering and handle quick pump out speeds if gases are needed to treat the surface of a sample.

We attempted to create fixed points on the cavity to further increase the resonant frequency, but became concerned about a mismatch between the coefficients of thermal expansion of the optical table and the glass rods supporting the optical cavity. As such, if the cavity was to be fixed to the table, baking the chamber could lead to the glass rods cracking under the induced stress. To circumvent this problem, we utilized kinematic mounts purchased from Bal-tec. One side of the cavity was mounted with two SS balls (750-TBR-T) constrained within tungsten carbide vee-blocks (VB-75-CPM), while the other side consisted of SS balls constrained by 45° tungsten carbide prismatic planes (45-DEG PP). This constrained overall movement in a Y configuration as shown in Fig. 2.14. We also attached standoffs machined out of PEEK material to act as thermal insulators to avoid undesirable heating of the main optical table.

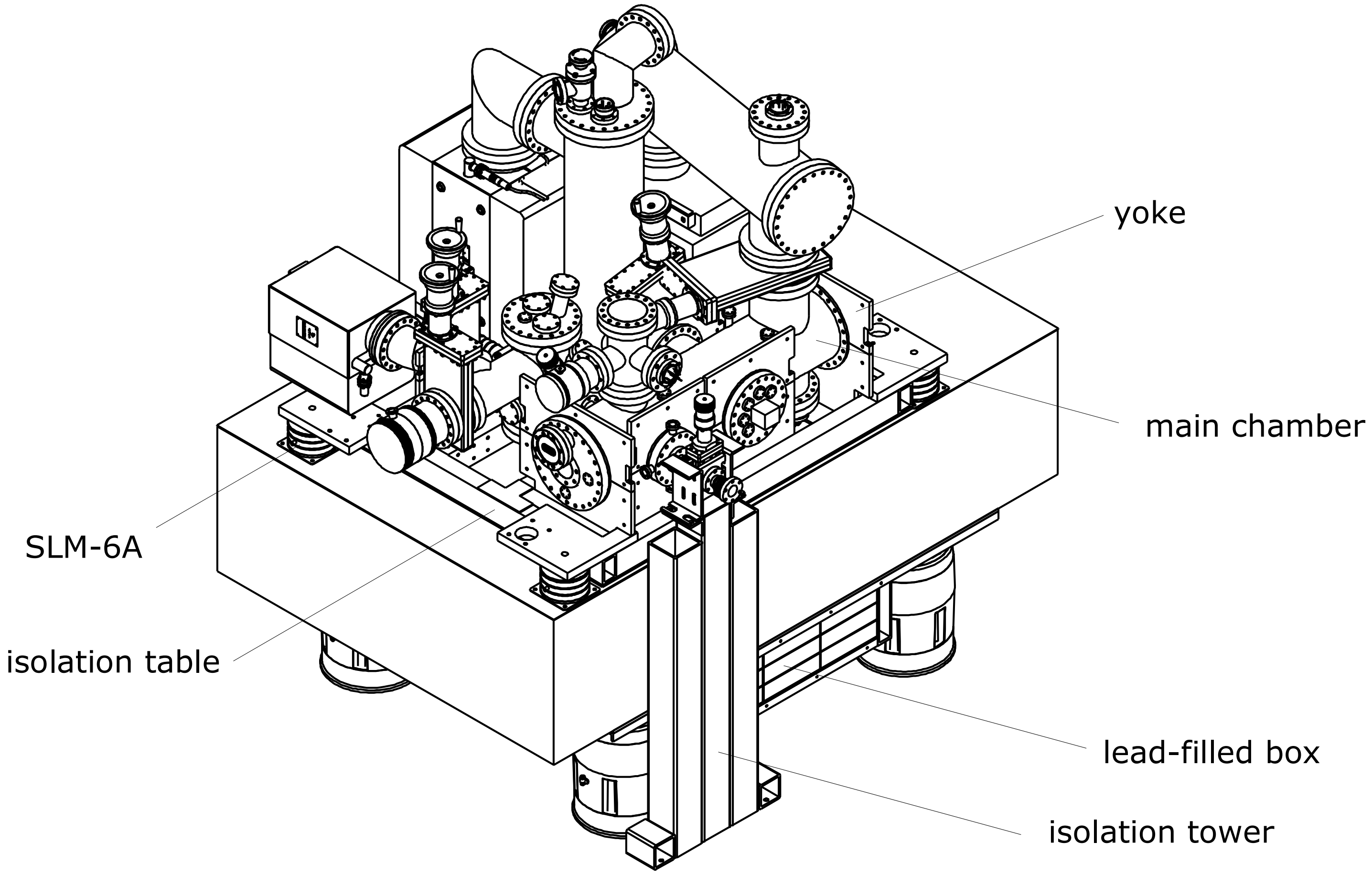

Figure 2.11: UHV apparatus in which Ps formation and excitation occurs with mechanical isolation components highlighted.

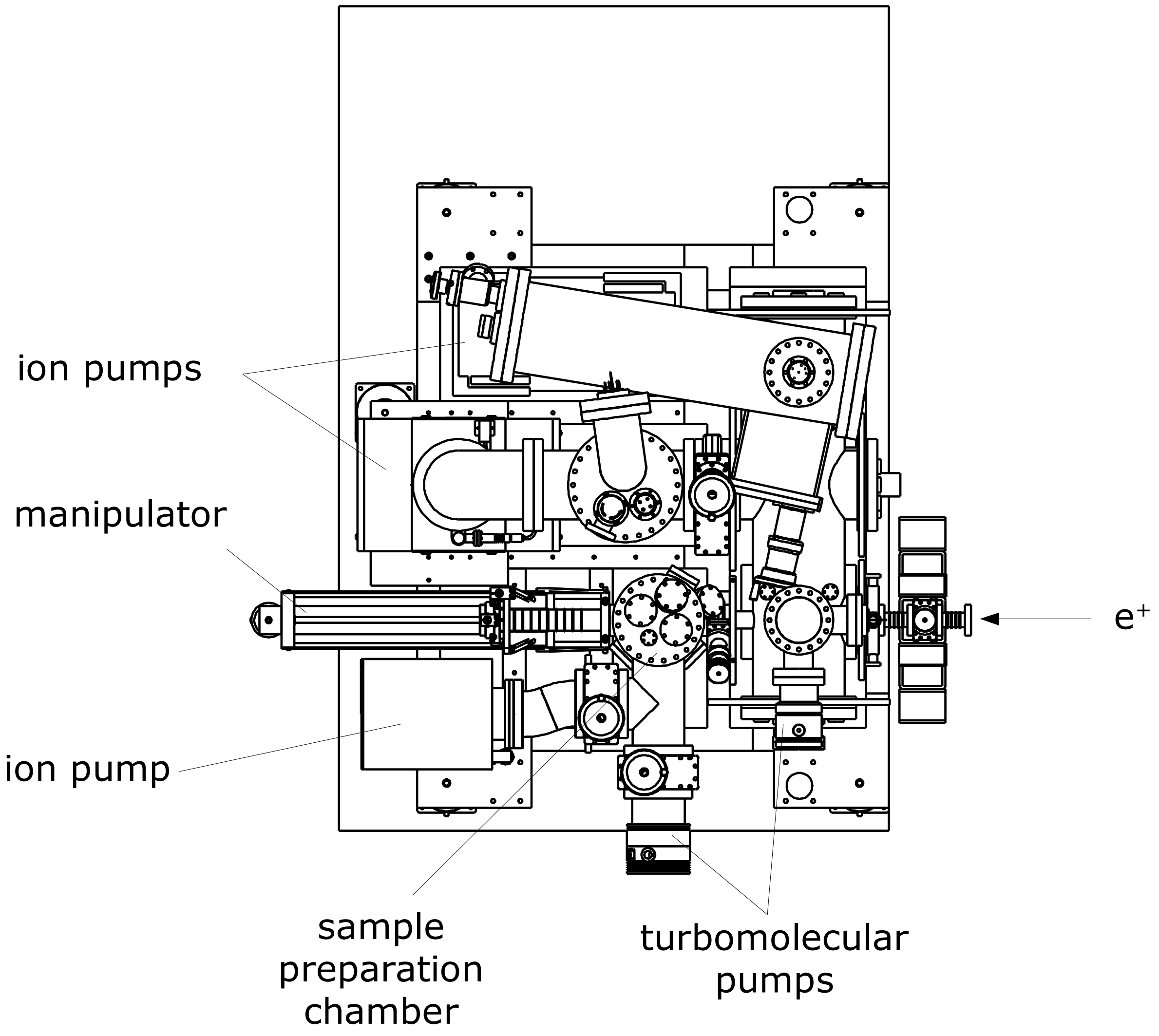

Figure 2.12: An overhead view of the UHV apparatus in which Ps formation and excitation occurs with vacuum components highlighted.

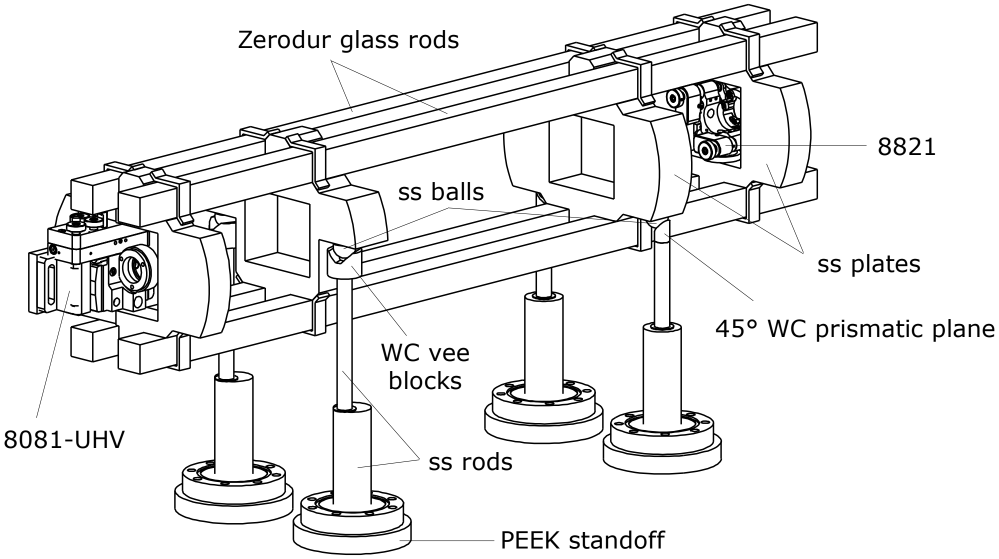

Figure 2.13: Optical cavity for two-photon excitation of Ps consisting of four Zerodur rods connected via stainless steel (SS) plates sitting upon SS rods.

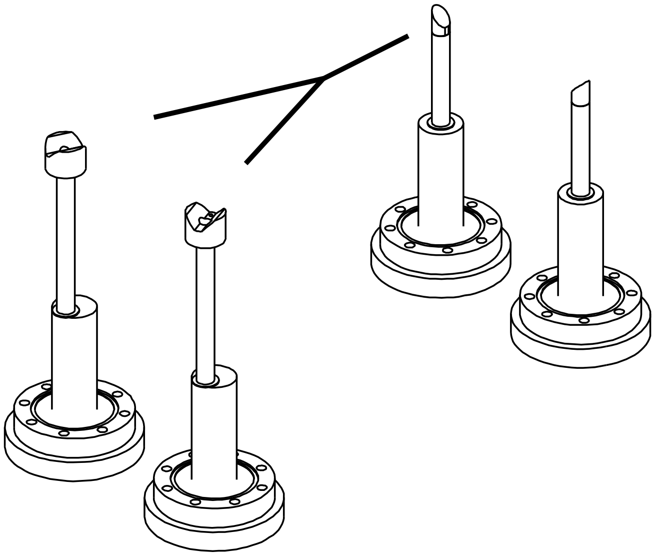

Figure 2.14: Kinematic mounts consisting of a pair of vee blocks and prismatic planes that constrain the movement of the cavity in a Y configuration without creating fixed points that could lead to problems due to a mismatch of coefficients of thermal expansion between the glass rods and stainless steel table.

The optical cavity, shown in Fig. 2.13, is constructed of 1″ square Zerodur rods connected by SS plates and brackets clamped with lead between. There are four such plates connecting the rods. Two of the plates are set at the $\lambda/4$ node of the rods to force the resonances to higher frequencies. These plates sit upon kinematic mounts that sit upon SS rods that provide a connection to the optical table through welded bellows. The other two plates connect only to the glass rods and house the mirror mounts and mirrors that define our cavity.

The cavity comprises two mirrors with radii of curvature of 50 cm and 20 cm, respectively. The mirror separation L is set to be ~ 69.2 cm, which corresponds to a free spectral range of 217 MHz. The mirrors were purchased from Advanced Thin Films who provided substrates superpolished to < 1 Å rms micro-roughness and guaranteed for >25000 finesse, but designed for >100000 finesse. With the laser locked to the main cavity, we can apply a low frequency, low duty cycle pulse to the laser diode current to briefly knock the laser out of resonance with the cavity in order to measure the ringdown time; we have measured the decay time τ to be $\sim 34\ \mu$s. This corresponds to a finesse of

$$\mathcal{F} = \frac{\pi c \tau}{L} \approx 46000 \tag{2.32}$$

Using the prescription from Sec. 2.2.1, with $P_{\text{inc}} = 437$ mW, $P_{\text{refl}} = 234$ mW, and $P_{\text{trans}} = 43$ mW, we calculate that the transmission loss is 23 ppm and the total loss due to scatter and absorption form both mirrors is 88 ppm. The transmission loss matches the specification of the manufacturer. The rest of the loss is due to mirror cleanliness: there is obvious scattering due to dust visible by eye. More work has to be done in order to keep the environment as clean as possible when mirrors are swapped out. An improvement in cleanliness of each mirror by a factor of 2 would bring the finesse up to nearly 90000. Based upon our measurement, the circulating power, as given by Eqn. 2.14, is 1.8 kW. At the target, where the beam radius ω is $\sim$850 μm, the intensity is 160 kW/cm^2.

The 50 cm mirror is mounted to a 5-axis motorized stage (Newport 8081-UHV) via a custom mirror holder. The 20 cm mirror is mounted to a two-axis stage (Newport 8821) in a custom barrel with two piezo actuators (Noliac NAC2125). The actuators have a maximum free stroke of 3.3 μm at 200 V. The mirror mounts allow us to align the mirrors remotely while the chamber is under vacuum. The 5-axis stage enables coarse changes to the length of the cavity, while the piezo actuators permit us to finely adjust the cavity length for scanning and tuning purposes.

The entrance breadboard setup is shown in Fig. 2.15. The beam is shaped twice: the first telescope shrinks the beam in order to pass through a Faraday isolator and EOM without clipping and the second telescope is for mode-matching to the cavity. The reference and reflected light is sent via optical fiber (Evanescent Optics, Inc. Corning PM48-U25D) to a balanced photoreceiver (Thorlabs PDB450A-AC) on the lowest gain setting. Since we cannot excite our atoms with circularly polarized light in our cavity, we must use a beamsplitter ($< 1\%$) to pick off our needed signals. The Faraday isolator and internal SHG cavity serve to protect the master oscillator from the reflected light, which can cause instability and destruction.

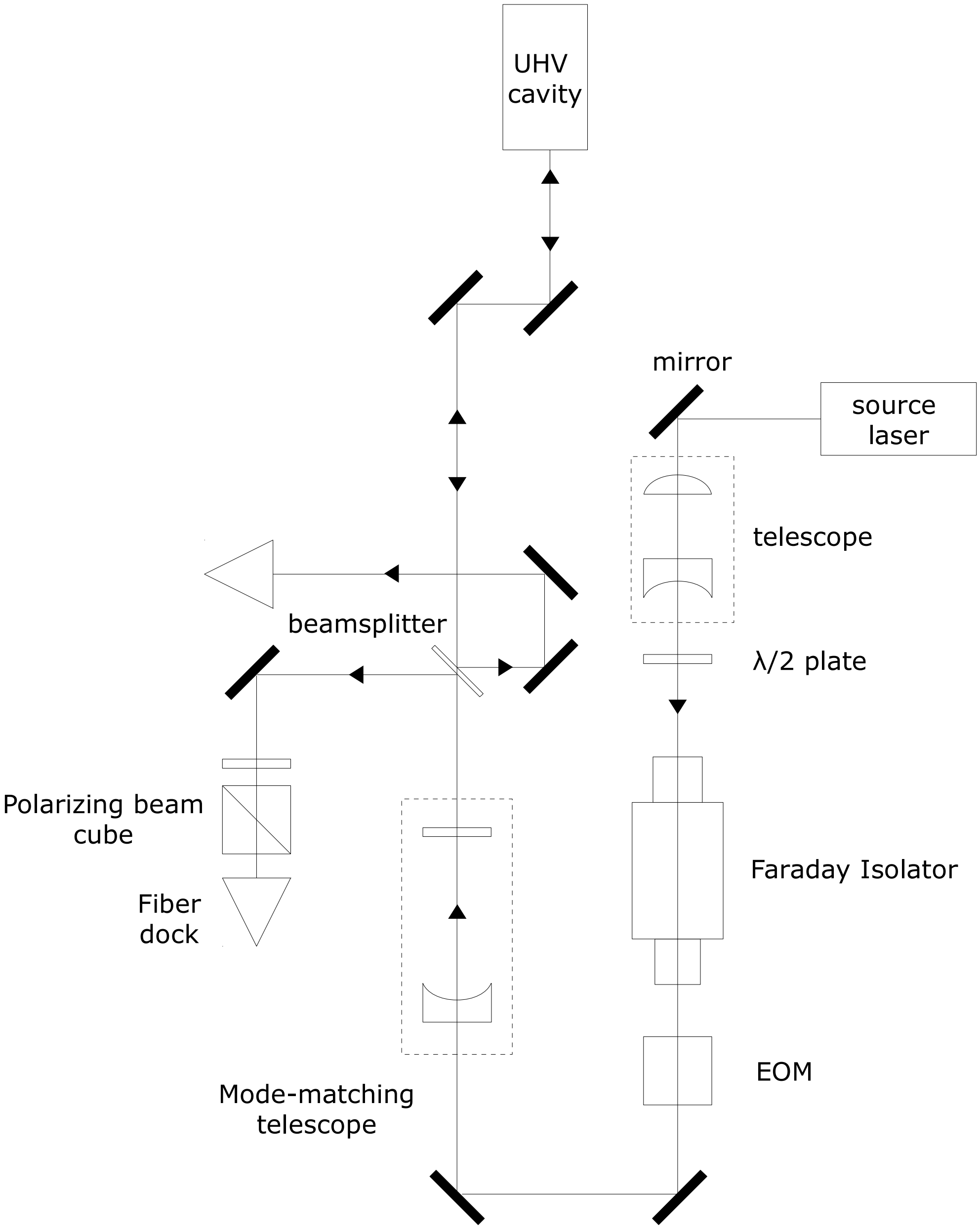

Figure 2.15: Schematic drawing of the breadboard at the entrance to the UHV chamber.

A second beam is used to excite the 2S Ps into Rydberg states where $n \geq 30$ to extend the atoms' lifetime such that they will survive until detection ∼30 cm away. The source of the ∼731 nm light is the same as described in Sec. 2.1.5. The light source is housed in a separate enclosure and brought in overhead via prisms and steered down from the top of the chamber, perpendicular to the 486 light. The light is aligned to the side of the 1S-2S interaction region in order to excite as much of the now 2S Ps distribution as possible.

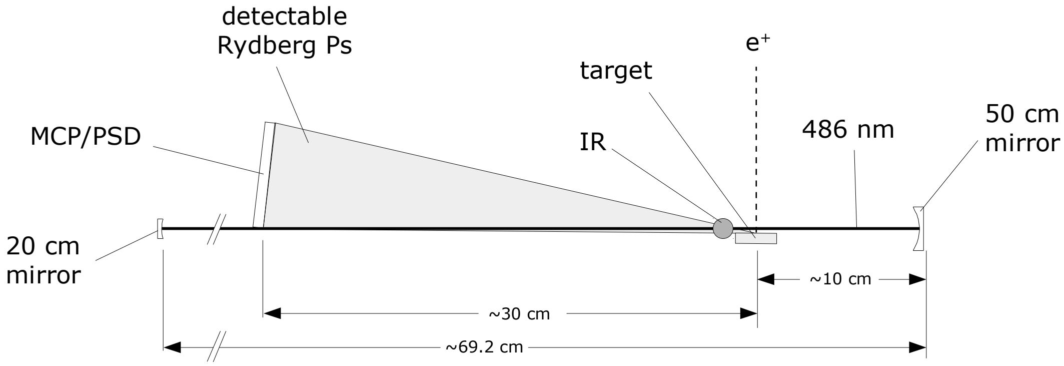

Figure 2.16: An overview of the primary components of the main excitation cavity. e^+ impinge upon the target and produce Ps, of which a portion are stimulated by 486 nm circulating light, resonant with the 1S-2S two-photon transition. Ps atoms in the 2S state are excited again via a one-photon transition to a Rydberg state, which extends the atom's lifetime long enough to reach a combination micro-channel plate/position sensitive detector. The position sensitive detector allows us to back out the trajectory of each atom in time and space.

2.4.4 Detection

The produced Rydberg atoms travel a distance of ~30 cm to a combination micro-channel plate (MCP) detector and position sensitive detector (PSD). In front of the MCP, incoming Rydberg Ps atoms are field-ionized [71] and the liberated positrons are collected. An electric field $|\vec{F}| \sim 10^6$ V/cm is generated between the front of the first MCP and a wire array suspended ~ 3 mm above it woven on a grounded plate. The wire array comprises 25 μm diameter tungsten wire aligned in a single direction and spaced ~ 1 mm apart for 98% transmission. The magnitude of the electric field and the low coverage of the wire array mean that there is substantial field leaking through in front of the intended ionizing region. This situation poses problems because the field can affect the incoming atoms in ways that obfuscate their original trajectory via steering in the field gradient or ionization of incident atoms outside of the detector. Modeling has revealed that atoms ionized prior to the detector are deflected < 1 mm. However, due to a stronger, curved field at the edge of the detector, positrons incident near the detector's edge are accelerated across the face rendering their trajectories unknowable [72]. These problems could be solved by using a higher density wire array to reduce leakage, which is desirable as Ps that is incident upon the near edge of the detector travels through a less intense portion of the 1S-2S excitation laser reducing the ac Stark effect. Another approach ameliorating this problem is to excite to lower Rydberg states where the photoionization limit is higher.

The now stripped and accelerated positrons are incident upon a Z-stack MCP, 75 mm in diameter. Each plate of the MCP comprises ∼35 million micro-channels, 10 μm in diameter, oriented at 8° relative to the surface normal; in a Z-stack, the channels are aligned to form a Z in the cross section. The angling of the channel plates with respect to one another helps reduce ion feedback [73]. Each channel acts as a continuous dynode that serves to amplify the signal of a single particle incident particle into a pulse of $\sim 10^7$ electrons [74].

The output of the Z-stack is deposited onto a $3.5''$ square indium-tin oxide coated glass resistive anode PSD that accurately determines the Cartesian position of the detected event [75] to better than ∼1 mm [76]. Thus, with a precise knowledge of from where the Ps atoms originate, limited by the e$^+$ beam focus to within $\pm \sim 100$ μm of the target center, and a measure of the detected position to ∼1 mm, we have complete picture of each atom's trajectory. Due to the Z-stack diameter and distance from the target, we collect atoms within a spread of 12°. Additionally, the ∼10 ns FWHM of the detected pulses, in conjunction with a narrow t_0 distribution (~ 30 ns FWHM at 5 keV implantation energy from a silica target [50]), allows for an accurate measurement of the time of flight. With expected flight times of 2-10 μs, the uncertainty in the flight time of an atom is known to $\leq 1.5\%$.

2.5 Metrology

2.5.1 Overview

The scheme for the metrology of the experiment was devised to obtain the highest accuracy and stability. Due to the expected acoustic and electronic noise on the excitation cavity, measuring the excitation cavity output directly against a frequency comb line would limit the precision of the measurement. In order to achieve the maximum precision out of the comb, we use an ultra-stable reference cavity to derive a steady, average frequency measurement. The frequency of light at the moment of excitation can then be measured with respect to the reference cavity to derive an instantaneous deviation due to noise on the excitation cavity thereby transferring the supreme accuracy and precision of the comb at the one second level into a sub-μs timescale.

2.5.2 Reference cavity

The reference cavity was purchased from Stable Laser Systems. The cavity assembly is ATFilms 6010-4, which is a premium grade, ultralow expansion (ULE), solid cylinder cavity assembly. A 50 mm in diameter and 100 mm long cylinder of ULE glass is axially center-bored and capped on either end with a plane mirror and a 50 cm spherical mirror to form a hemispherical optical cavity. Each mirror is superpolished on the cavity-facing side and has an anti-reflective coating on the other. Another bore connects perpendicularly to the axial bore to allow the cavity to be pumped down to vacuum.

The cavity is mounted in a vacuum housing also supplied by Stable Laser Systems for thermal stability and cleanliness. The temperature is actively controlled (Wavelength Electronics, Inc. LFI3751 5A), stable to ±0.01 °C and set to correspond with the zero-crossing temperature of the ULE spacer 58.35°C . Due to the active heating of the unit, typical pressures are 10^{-8} torr using a 10 L/s ion pump through a mini-CF tee on the 261 mm long by 190 mm diameter can.

In order to lock to the reference cavity while simultaneously locking to the main excitation cavity, we employ two acousto-optic modulators, both operating in a double-pass configuration. The first AOM (AOM1, IntraAction Corp. ADM-402AF1) imparts a modest frequency shift, currently centered at 40 MHz in single pass, but primarily maintains the lock to the reference cavity also via the PDH method with sidebands imparted at ±45 MHz by EOM: the fast part of the error signal derived from the stable cavity is fed to AOM1. This serves to provide correction to the high frequency noise from the UHV system that is imparted to the cw beam as it stays locked to the main cavity. Some of the light that has been stabilized from AOM1 is picked off and sent to be beat against the main excitation cavity output in order to ascertain the instantaneous excursion of the light's frequency during the interaction time.

The beat note will be measured on an oscilloscope (Keysight DSOS054A). The scope has a two-channel sample rate of 20 GSa/s and 10 bit resolution. Instead of detecting and analyzing the beat note on a spectrum analyzer, we will download the trace and fit the curve. The time window will span two ground state lifetimes (2×142 ns) and the expected beat is on order 80 MHz ± 200 kHz. We have tested this scope with the 80 MHz signal

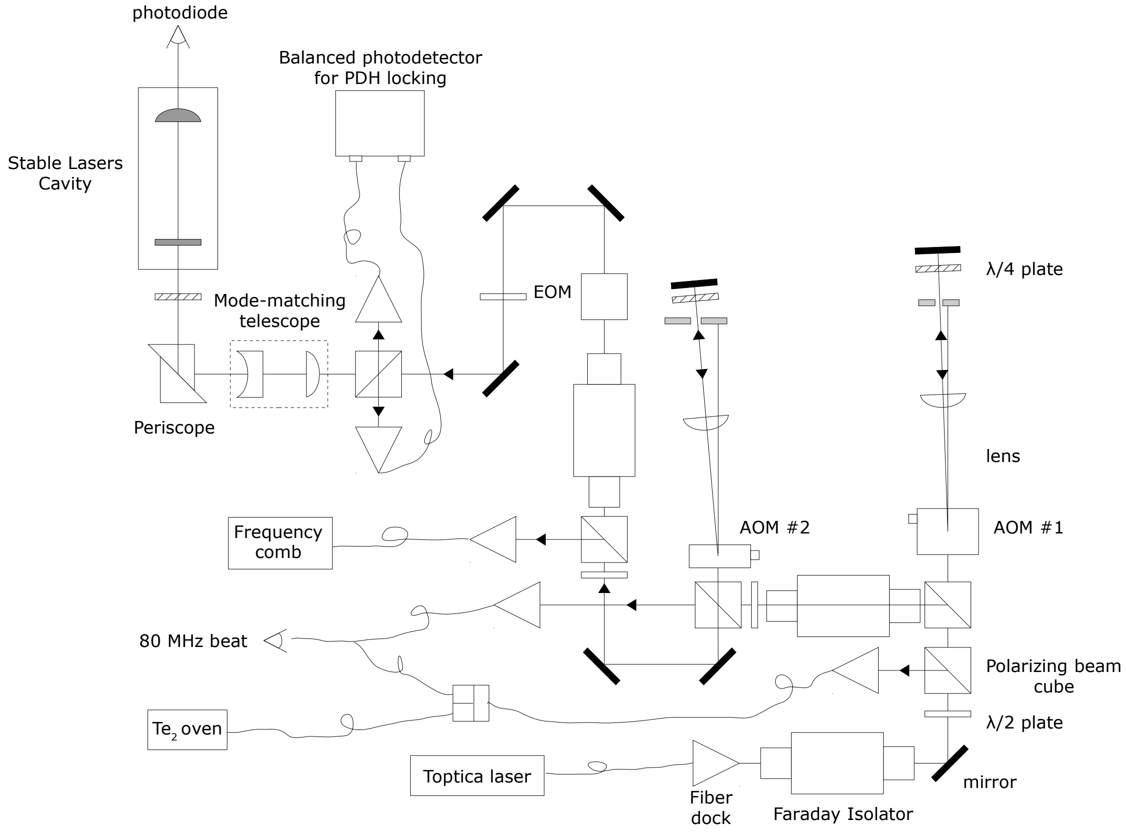

Figure 2.17: Schematic of the reference cavity breadboard.

The slow part of the error signal from the reference cavity lock is fed to the piezo of the excitation cavity. This slow feedback is essential to maintaining a double lock to the main and reference cavities simultaneously because it corrects the drift of the main cavity to stay near the reference cavity resonance. We have seen the main cavity line center jitter around 2.5 MHz.

The slow feedback also provides the mechanism for tuning through the desired resonance, which is carried out by tuning the frequency of the second AOM (AOM2, IntraAction Corp. ATD-2001A1). By slowly changing the frequency of AOM2, the slow feedback changes the length of the main cavity via its piezo. In addition to providing the mechanism for tuning, AOM2 shifts the cw beam frequency the rest of the way into resonance with the reference cavity with a center frequency around 200 MHz in single pass. Part of the light that has double-passed AOM2 is picked off and sent to the frequency comb to be measured and provide the average frequency measurement. We use the light before the cavity as opposed to that which is transmitted because we have limited light to send to the reference cavity such that the transmitted light intensity is quite low.

We have measured the finesse of the reference cavity via its ringdown time to be $\sim$66000 indicating a linewidth of $\sim$23 kHz. The decay time was $\sim 6\ \mu$s. While we had hoped to achieve a finesse of 10^5, it is possible that the mirrors were dirtied during the installation process.

The reference cavity lock will be continuously monitored for dropouts, which are periods where the transmission of the cavity is below a certain threshold for time spans on order of the decay time. This indicates that the frequency of the main cavity is unstable and the reference cavity is dumping out light at a similar rate that it is filling it with light. This places a large uncertainty on the frequency stored in the main cavity during this period and data collected during this interval must be thrown out.

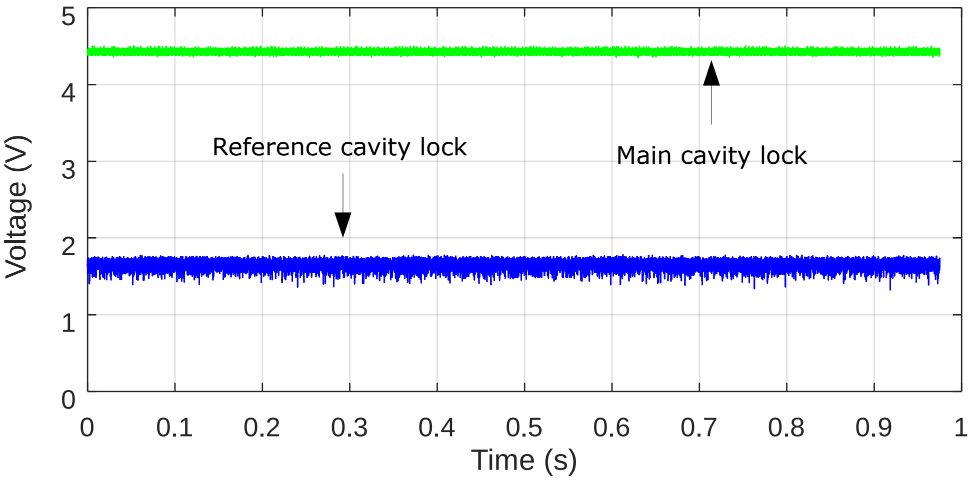

Figure 2.18: A simultaneous lock of both the main excitation cavity and the reference cavity.

We have achieved a simultaneous lock of both the main excitation cavity and the reference cavity, shown in Fig. 2.18. Based upon the linewidth of the main excitation cavity, as determined by the finesse, and thickness of the trace of our lock, we estimate the laser to be holding within 200 Hz. However, the lock is clearly not as tight to the reference cavity; it appears to be within 7 kHz at best. This indicates that while the resonance of the main cavity is narrow, it is moving about on order of 2.5 MHz. AOM1 can only correct to the absolute maximum of 2.6 MHz. While a complete dropout, i.e. a point at which the light in the reference cavity completely drains, is not seen, in a zoomed in picture, one can see the issue at hand. In Fig. 2.19, a zoomed in view of both locks is shown. While no significant dropout is seen in the main cavity lock, the narrow-looking dropouts in the reference cavity are on order of 100 μs. Because the transmission does not go to zero, the reference cavity is tracking the main cavity, but the main cavity is moving around too much for the reference cavity to build up. The center frequency of the main cavity is bouncing around such that the reference cavity is dumping light about as quickly as it is filling. There is more that can and is being done to further mechanically stabilize the positron apparatus, which will help quiet the main cavity. However, as long as the dropouts are monitored and data acquired during these moments is thrown out, there are enough times during which the cavity is stable and the data meaningful for preliminary experiments to occur.

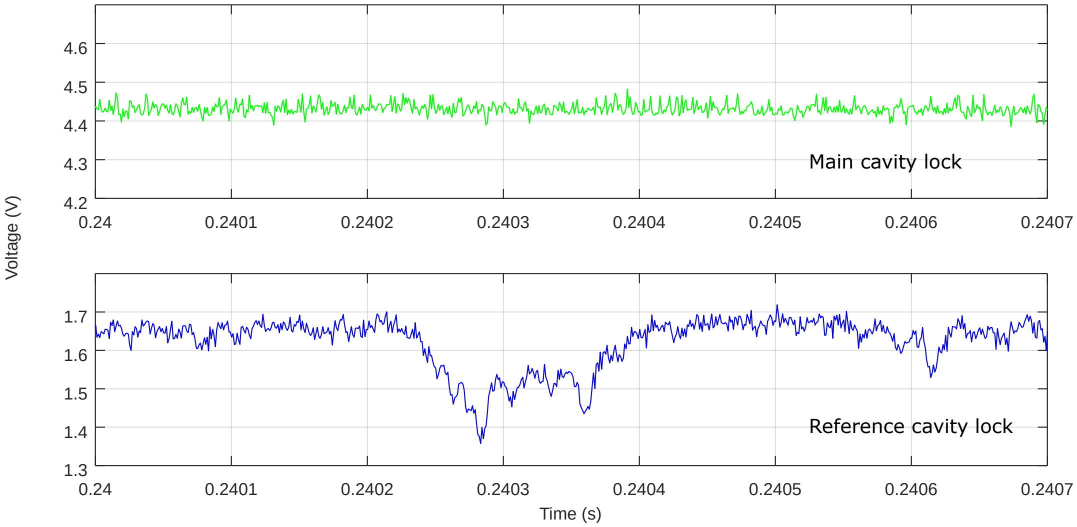

Figure 2.19: A zoomed in view of the simultaneous lock of both the main excitation cavity and the reference cavity.

2.5.3 Frequency comb

In order to measure the frequency of our cw beam, we must have a stable, reliable reference against which we can compare. The ultimate way to accurately and precisely measure the frequency of light is using a frequency comb. A frequency comb is a tool that is like a ruler for light with lines of fixed frequency and fixed spacing.

The starting point of a frequency comb is a coherent, broadband source of light. The Heisenberg uncertainty principle dictates that a temporally short pulse of coherent light must have a proportionately broad bandwidth. A periodically pulsed femtosecond laser thus forms the basis of a frequency comb, producing a stable series of equally spaced peaks in frequency ω, as shown in Fig. 2.20.

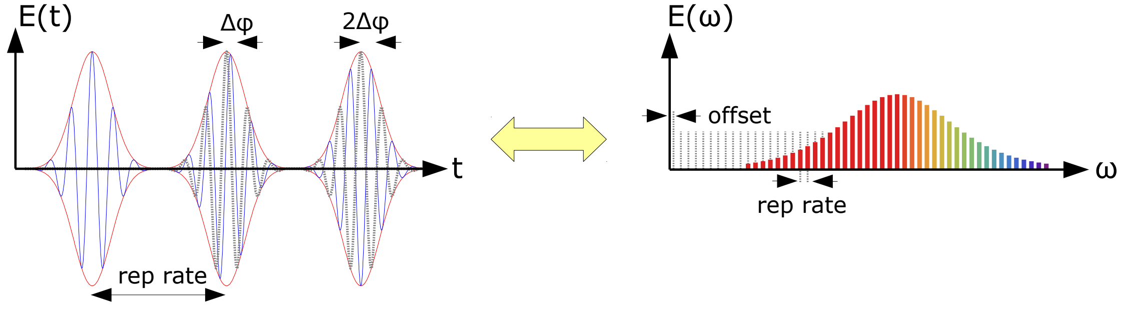

Figure 2.20: Relationship between pulsed electric field and comb modes.

Each finger of the comb is at a well defined position and has frequency determined by three variables

$$f_{\text{comb}} = n f_{\text{rep}} \pm f_{\text{ceo}} \tag{2.33}$$

where n is an integer number, f_{rep} is the repetition rate of the laser, and f_{ceo} is the carrier envelope offset frequency. The f_{rep} is a function of the cavity length and thus the round trip time of a pulse, $T = 2L/\upsilon_g$, where υ_g is the group velocity. The f_{ceo} is the frequency domain result of the phase difference $\Delta\phi$ between the fast carrier signal slipping under the slow pulse envelope in the time domain due to the difference in the group and phase velocities.

When a cw beam is beat against a comb line the frequency of the measured source is f_{cw}

$$f_{\mathrm{cw}} = nf_{\mathrm{rep}} \pm f_{\mathrm{ceo}} \pm f_{\mathrm{beat}} \tag{2.34}$$

Through stabilization of the f_{rep} and carrier offset frequencies and measurement of the comb mode number, we can reliably and accurately know the frequency of our light.

We have purchased a frequency comb from Menlo Systems, Inc. that works in the following way. A femtosecond pulse is generated from an erbium-doped fiber laser centered at 1560 nm spanning 25 nm with a mode spacing of 250 MHz. This is fed into a highly nonlinear fiber to generate an octave spanning continuum from approximately 1 μm to 2 μm.

A mode number in the red portion of the spectrum is then frequency doubled

$$f_1 = nf_{\mathrm{rep}} + f_{\mathrm{ceo}} \tag{2.35}$$

$$f_2 = 2nf_{\mathrm{rep}} + f_{\mathrm{ceo}} \tag{2.36}$$

and beat against a mode number a full octave away

$$2f_1 - f_2 = f_{\mathrm{ceo}} \tag{2.37}$$

which yields the carrier envelope offset, typically set and held at 60 MHz with Allan variance (AVAR) < 100 mHz. The details of the AVAR will be discussed later.

The mode spacing, or repetition rate, is held fixed in the following manner. The fourth harmonic of the f_{rep} is mixed with the output of a phase locked oscillator (PLO) at 980 MHz to produce a beat note around 20 MHz. The f_{rep} is then stabilized through feedback to the cavity piezo to adjust the cavity length. The f_{rep} is tunable over a large range, such that without a sub-125 MHz wavemeter, we can take two measurements of our cw beam against comb lines that are separated by a large integer mode number to ultimately extract n_1,

$$n_1 = \frac{\Delta f_{\text{ceo}} + \Delta f_{\text{beat}}}{\Delta f_{\text{rep}}} + \frac{m f_{\text{rep2}}}{\Delta f_{\text{rep}}} \tag{2.38}$$

where Δf_{ceo} is the difference between the two carrier offset frequencies, Δf_{beat} is the difference between the two beat frequencies measured, $m = n_2 - n_1$ is the integer mode difference, and Δf_{rep} is the difference between the two repetition rates used. Typically $\Delta f_{\text{ceo}} = 0$ and the repetition rates can be chosen such that the beat frequencies also cancel.

In a separate path, the 1560 nm is also frequency doubled to move the spectrum to the visible range[1]. The generated 780 nm light is coupled into a photonic crystal fiber (PCF) to create a supercontinuum in the visible range. Unfortunately, the portion of the light we care about is in the wings where the intensity is low. We have tried to improve the signal-to-noise ratio of the beat note through a design of our own (see Fig. 2.21) in order to achieve best possible mode-matching conditions and isolation of the important mode.

---

[1] Due to this doubling, when measuring the frequency of our light, we must add a factor of two in front of the carrier such that $f_{\text{cw}} = n f_{\text{rep}} \pm 2 f_{\text{ceo}} \pm f_{\text{beat}}$.

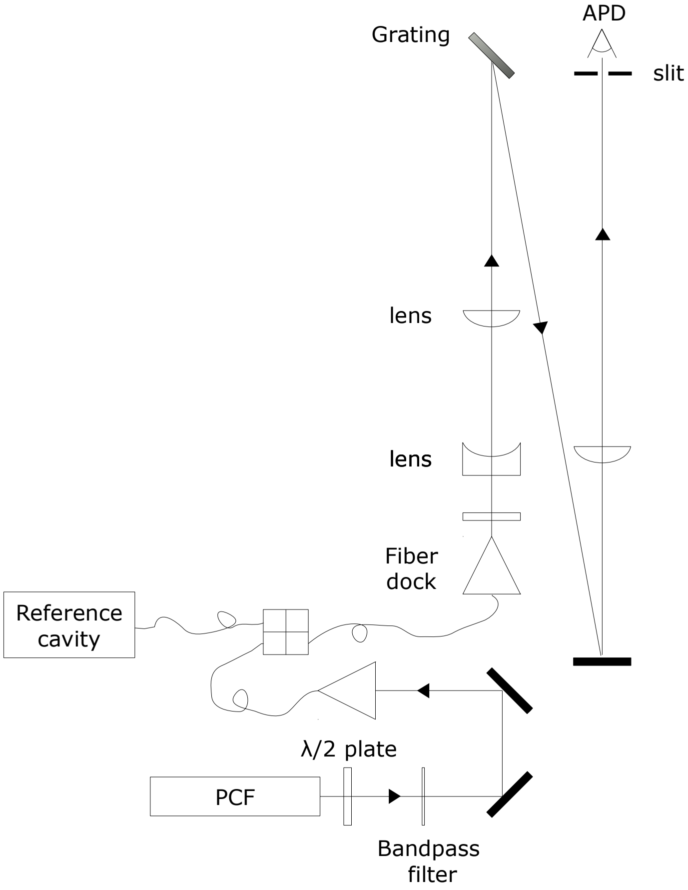

Figure 2.21: Schematic of frequency comb breadboard.

After the PCF, the light passes through a bandpass filter, 10 nm wide and centered at 486 nm, before being coupled into one of our fibers. The output of the fiber emits 90% of the comb light and 10% of the light locked to the reference cavity. This collimated light is telescoped up and incident upon a near-Littrow grating (Richardson, 3600 lines/mm) located at the beam waist as measured with a shear interferometer. The diffracted light is then focused with a lens through a slit onto an avalanche photodetector. We reliably achieve 20 dB signal-to-noise ratio (SNR) with a FWHM of around 300 kHz.

Our comb has the capability of optically locking whereby f_{rep}, instead of deriving its lock signal from mixing with the PLO, is beat against and stabilized to the cw laser. Because the comb is now tracking the frequency of the beam to be measured, and due to the fact that the signals for locking are derived from optical frequencies, the beat note is an order of magnitude smaller at ~ 30 kHz. Unfortunately, in order to utilize this capability, we need a SNR that is reliable and continually > 30 db. This is very difficult to achieve and maintain due to the low intensity of light at the required comb line and has not proven robust enough for our utility.

2.5.4 Reference clock

The reference clock we are using for all equipment requiring or desiring such a signal is the Meridian II Precision TimeBase from EndRun Technologies. It is a GPS-disciplined, ultra-stable double-oven-controlled crystal oscillator that provides a 10 MHz signal to eight different outputs. The temperature stability of the oven is a part in 5×10^{-10} between $-20\,^{\circ}$C and $70\,^{\circ}$C.

The single sideband (SSB) phase noise of the 10 MHz output at 1 Hz is -113 dBc/Hz. The SSB phase noise is a measure of the frequency stability of the clock. Phase noise affects when the zero crossing of the sine wave occurs and it is equivalent to a frequency shift.

In order to characterize the frequency stability of oscillators and clocks, we use the Allan variance (AVAR, $\sigma_y^2(t)$), also known as two-step variance [77]. The AVAR is derived by comparing two devices, one as a reference and one under test. It is used to characterize stochastic noise in a system but not systematic error and drift. The device being tested is compared at an interval $i\tau$ and $(i+1)\tau$ and an average is taken such that

$$\sigma_y^2(\tau) = \frac{1}{2(M-1)} \sum_{i=1}^{M-1} (y_{i+1} - y_i)^2 \tag{2.39}$$

The fractional frequency is

$$y_i = \frac{\langle \nu_1(t_0 + i\tau) \rangle_\tau - \nu_0}{\nu_0} \tag{2.40}$$

where ν_0 is the frequency of the reference and $\langle \nu_1 \rangle_\tau$ is the tested device's frequency averaged over the time interval τ. The Allan deviation (ADEV) is simply $\sqrt{\sigma_y^2(\tau)}$. The ADEV for the timebase we are using is plotted in Fig. 2.22 from data provided by the manufacturer [78].

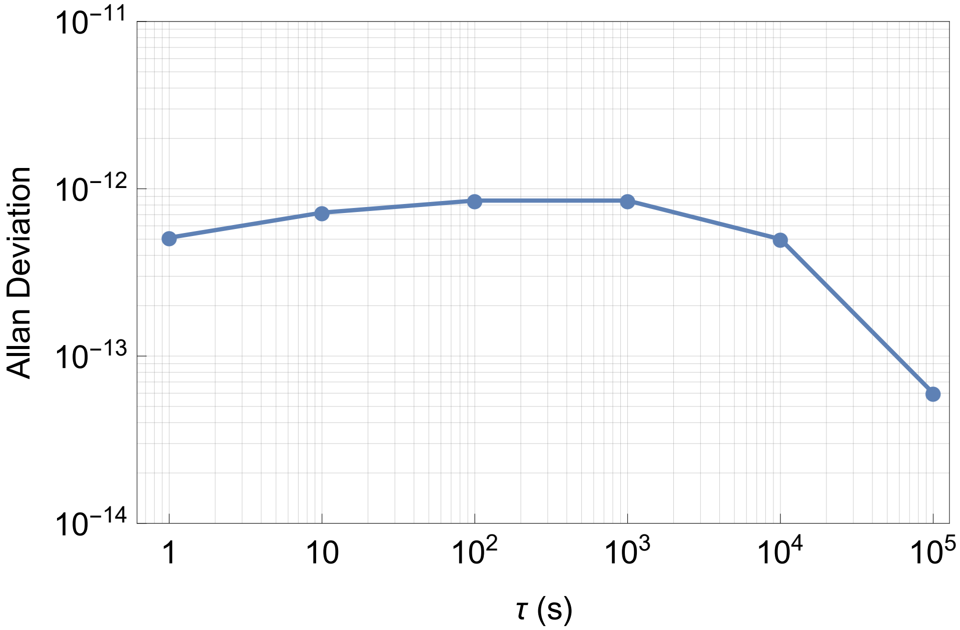

Figure 2.22: Allan deviation for the Meridian II TimeBase based upon the manufacturer's data.

2.5.5 Tellurium spectrometer

Tellurium is a useful atomic reference due to its high density of strong spectral lines that span from nearly 400 to 1400 nm [79]. In particular, the so-called e_3 line of $^{130}Te_2$ is within 200 MHz of half of the 1S-2S interval frequency. The tellurium oven we constructed was completed before we had received funding for a frequency comb. While it will no longer be required on a daily basis, it is useful for quickly aiding in finding the correct order of our reference cavity and as a back up in the event the frequency comb faces significant downtime.

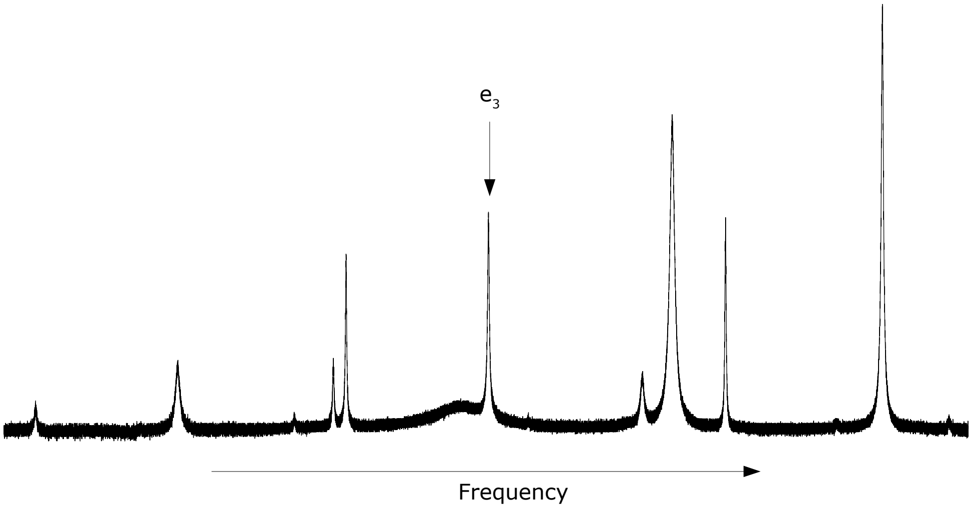

Figure 2.23: A spectrum of $^{130}Te_2$ taken from our oven with the e_3 line denoted and an arrow indicating the direction of increasing frequency.

We constructed our oven, illustrated in Fig. 2.24, around a quartz cell containing $^{130}Te_2$. The cell purchased from Opthos Instruments, Inc. has a 25 mm diameter, 100 mm long body with a 70 mm long stem; these are the same dimensions as Fee et al [20]. The oven consisted of a 10 inch vacuum tee that was chosen to accommodate thermal insulation and allow us to operate at low pressure for more thermal isolation, if desired. We used clam-shell type heaters custom produced by Thermcraft, Inc. that consist of iron-chrome-aluminum wire embedded in ceramic fiber. The wire is wound helically, which reduces solenoid-like effects, i.e. non-inductively wound. Two long quartz sleeves were placed over the cell on either side to help prevent contaminants from settling on the cell windows. An aluminum cylinder was slid over the stem to aid in keeping the entire stem a single temperature. Thermocouples were placed at various locations in order to measure the stem and body temperatures. The thermocouples were homemade K-type made from 0.005″ alumel and chromel wire spot welded together and sheathed with insulation.

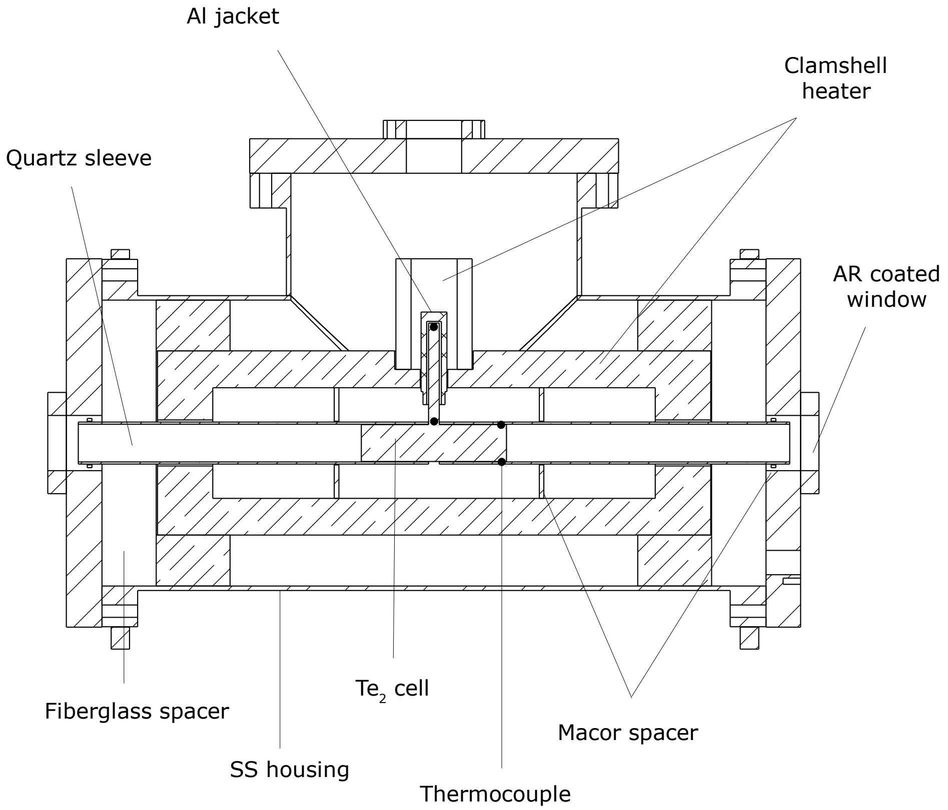

Figure 2.24: Oven used to heat $^{130}\mathrm{Te}_2$ cell used as an atomic reference.

We use a single temperature controller (Omega CN32Pt-440) and two variacs to set and hold the temperature of the cell at the desired level to ±1 °C. The controller provides the main switching of power on and off to the heaters. The upper clam shell is supplied by 120 V from the wall. The bottom clam shells are provided with a percentage of wall power determined by the setting of each shell's variac. The variacs are set to keep the body temperature at a level hot enough to prevent the atoms from sticking to the cell windows while not creating too large of a temperature gradient, which would risk cracking the quartz cell.

The difficulty in reproducing ovens with identical temperatures at identical locations means that a temperature prescription is not enough to guarantee results from one oven to another. The temperature that is most important is the effective cold point, as this sets the vapor pressure and thus the linear absorption of the system. Therefore the current prescription is to set a cold point temperature that produces absorption of 30%, presumably at the peak of the e_3 line, although this is never stated explicitly in the literature. It was shown that linear absorption is not as sensitive to the body temperature; a rise of 110 °C increased the absorption by only 5% [80]. Various discrepancies in measurements of the e_3 line appear to have been resolved based on corrective scaling such that the frequency measured is based upon the same vapor pressure by taking into account erroneous temperature measurements and different sized cells [20]. It should be noted that the vapor pressure is never directly measured in any of these results, but is instead inferred based upon temperature [81]. If we compile all of the previous work, the e_3 frequency is 616803545.25 ± 0.64

MHz [20,80,82,83]. This is 63.8 MHz below the two-photon transition frequency as measured by Fee et al [20].

A fraction of our source laser light was picked off and sent to the oven setup some distance away via fiber and employed in a Doppler-free saturated absorption spectroscopy scheme, illustrated in Fig. 2.25, to observe the $^{130}\mathrm{Te}_2$ spectrum. The beam was split three ways to provide two probe beams, signal and reference, and a counterpropagating pump beam. The pump beam is passed through an AOM (IntraAction Corp. AFM-602A20) where it is shifted by −60 MHz and chopped at 120 kHz from a Time-Base DIM-3000 driver that is referenced to our 10 MHz clock and directed to the cell. The AOM shift means that the e_3 line will be shifted −30 MHz such that $f_{e3} = f_{\mathrm{laser}} - 30$ MHz.

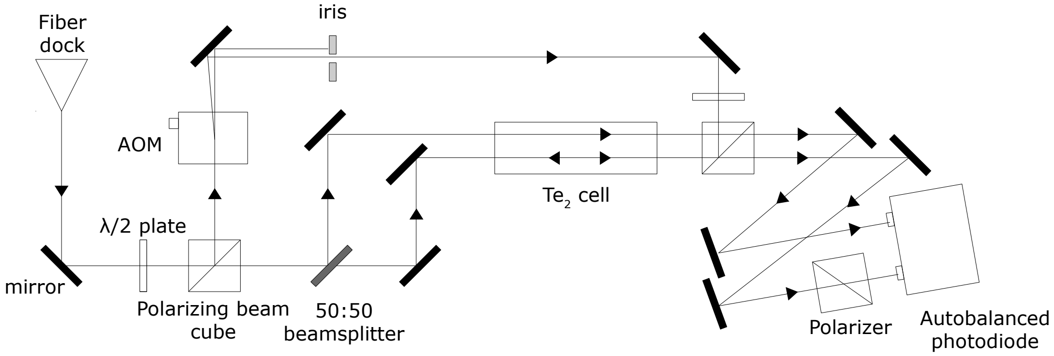

Figure 2.25: Schematic of the Doppler-free saturated absorption spectroscopy of Te_2 breadboard.

The probe and reference beams pass through the cell and are detected on an autobalanced photoreceiver (Newport Nirvana 2007). The signal beam is attenuated just prior to the detector to create a reference-to-signal ratio of ∼2:1 as required by the device. We used the highest gain and bandwidth settings for best results. The linear output of the detector is sent to a lock-in amplifier (Signal Recovery 7265), which also provides the chop signal. The power of each beam was measured before and after the oven with the oven temperatures as measured below with a variation of $\pm 1\,^{\circ}$C:

The signal and reference beams were ~ 1 mW, while the pump beam was ~ 3.20 mW, and all beam sizes were approximately the same at $\omega = 530$ μm. This implies power densities of 227 mW/cm^2 and 725 mW/cm^2 for the probe and pump beams respectively.

2.6 Uncertainty budget

Below is a summary of the major contributions to uncertainty in the projected measurement of the $1^3S_1 - 2^3S_1$ interval of Ps. A tabulation of the values is presented in Table 2.1.

Second-order Doppler shift

The uncertainty in the second-order Doppler shift is dependent upon the velocity of the detected atoms. We will determine the velocity of each particle from where it was detected on the PSD and at what time relative to t_0. For now, the uncertainty in the time of flight is dominated by the time width of the Ps emission. Additional uncertainty is attributed to our measurement of the mean time of the direct annihilation prompt peak, the time resolution of the implanted positron pulse, the jitter in our start gate trigger, and the time elapsed between ionization of the Ps at the detector to collection of the positron on the front MCP. The relatively slow emission of Ps from the silica (~ 30 ns, FWHM) dominates the cumulative uncertainty.

An atom with a speed of $\sim 8 \times 10^4$ m/s, the expected average speed for room temperature atoms emitted from silica, will travel 30 ± 0.5 cm from the target to the detector in $< 4 \pm 0.015$ μs. This corresponds to a second-order Doppler shift of $\sim 24 \pm 0.8$ MHz.

ac Stark shift

The uncertainty in the ac Stark shift is due to the intensity through which the atom traverses. Due to our PSD accuracy of ~ 1 mm and stable power output, the shift will contribute $< 7\%$ uncertainty, or around 80 kHz at our current intensity of ~ 160 kW/cm^2. The ac Stark shift can also be exactly found for each atom by changing the laser intensity and extrapolating back to zero field.

Average frequency

The average frequency is the frequency of the stable reference cavity as measured by the frequency comb. The beat note produced is ~ 500 kHz and will be averaged over the time spent at a given frequency as we scan across the 1S-2S resonance and then fit to determine the center. A fit of this data will provide < 10 kHz uncertainty.

Instantaneous frequency

The uncertainty in the instantaneous frequency measurement is dominated by the stability of our cavity. Noise due to vibration from the lab environment is clearly seen on the jitter of the line center, < 3 MHz, and ringing at 250 Hz is seen on the laser as it follows the cavity. The 250 Hz is likely a resonance of the optical table, which may be reduced by covering the table in acoustic foam and adding baffles to reduce turbulence in the air within our enclosure. Further securing the e^+ beam will go a long way towards reducing the largest noise.

As described earlier, the main cavity output will be beat against the beam filtered after double-passing AOM1, and captured on an oscilloscope. We will record for twice the lifetime of the triplet ground state, 2×142 ns, which will determine the instantaneous frequency offset during the interaction time. The quality of our fit is determined by the sample rate and number of bits displayed. We have tested the oscilloscope on 1 μs periods with an 80 MHz signal and found a standard deviation of 1 kHz on the same order as the confidence interval.

AOM offset

There is some uncertainty associated with the static AOM, AOM2. It is referenced to our 10 MHz clock, which has an Allan variance of 10^{-12} at the 1 s interval. In double pass, AOM2 frequency shifts the beam by ~ 400 MHz. The uncertainty associated with this offset is related to the quality of the lock. If we can only stay locked to within 5% of the resonance for 1 ns, our uncertainty is $10^{-12}/10^{-7} \times 400\ \mathrm{MHz} = 4$ kHz; a quality lock over 50 μs yields an uncertainty of 8 Hz. At the current level of precision, this will have no significant contribution to our overall uncertainty.

Table 2.1: Projected uncertainties in measurement of the $1^3S_1 - 2^3S_1$ interval of Ps in units of kHz.

Source	σ(kHz)
2nd-order Doppler shift	800
ac Stark shift	80
average frequency	10
instantaneous frequency	1
Total	804

2.7 Conclusion

We have designed and constructed an apparatus to enable ultrahigh precision measurements at sub-μs timescales, a new frontier in atomic spectroscopy. Our apparatus will measure the $1^3S_1 - 2^3S_1$ of Ps to a precision of $\sim$800 kHz in the first round of experiments. This precision is a factor of 2 improvement over the previous best measurement.

Currently, the second-order Doppler shift greatly dominates the uncertainty in a measurement. Its impact can be diminished primarily in three ways: (1) by simply counting for longer, we can accrue more counts from the slowest population of emitted Ps, but as this will sit far to the side of the peak in the distribution, the count rate will be low; (2) the uncertainty is proportional to the time of flight such that a 2× longer flight path produces 2× lower uncertainty; (3) using a target that can produce thermal Ps at temperatures around 100 K, such as Al(111), the uncertainty will be a factor of 3× lower. As the uncertainty of the second-order Doppler shift is reduced, the contributions from other sources will become more prominent and will have to be considered and addressed accordingly.

The ultimate goal, a direct comparison of the QED terms in hydrogen and Ps, is possible at the 1 kHz level of precision, which will require great attention to reducing the systematic and statistical uncertainties as well as long collection times. At such a precise level, experiment will have progressed beyond the current theoretical calculations. Presently, the theoretical calculations and experimental measurement of the 1S-2S interval differ by almost 2σ, a possible sign of some disagreemtn, but not a statistically unreasonable deviation. At a precision comparable with that of the complementary hydrogen spectroscopy, i.e. a part in 10^{-15}, it will be evident if Ps has its own issues of disagreement that need to be resolved.

The future is uncertain but exciting, and the continual improvement of the apparatus and the spectroscopic data produced from it will contribute greatly to our knowledge of fundamental physics.

Bibliography

[1] C. D. Anderson, "The positive electron," *Phys. Rev.*, vol. 43, pp. 491–494, Mar 1933.

[2] "A theory of electrons and protons," *P. Roy. Soc. Lond. A Mat.*, vol. 126, no. 801, pp. 360–365, 1930.

[3] "Quantised singularities in the electromagnetic field," *P. Roy. Soc. Lond. A Mat.*, vol. 133, no. 821, pp. 60–72, 1931.

[4] S. Mohorovičić, "Mglichkeit neuer elemente und ihre bedeutung fr die astrophysik," *Astronomische Nachrichten*, vol. 253, no. 4, pp. 93–108, 1934.

[5] M. Deutsch, "Evidence for the formation of positronium in gases," *Phys. Rev.*, vol. 82, pp. 455–456, May 1951.

[6] A. P. Chu, Steven andMills, Jr., "Excitation of the positronium $1^3S_1 \rightarrow 2^3S_1$ two-photon transition," *Phys. Rev. Lett.*, vol. 48, pp. 1333–1337, May 1982.

[7] A. M. Alonso, B. S. Cooper, A. Deller, S. D. Hogan, and D. B. Cassidy, "Positronium decay from $n = 2$ states in electric and magnetic fields," *Phys. Rev. A*, vol. 93, p. 012506, Jan 2016.

[8] R. Ley, D. Hagena, D. Weil, G. Werth, W. Arnold, and H. Schneider, "Spectroscopy of excited state positronium," *Hyperfine Interact.*, vol. 89, pp. 327–341, Dec 1994.

[9] W. E. Lamb, Jr. and R. C. Retherford, "Fine structure of the hydrogen atom by a microwave method," *Phys. Rev.*, vol. 72, pp. 241–243, Aug 1947.

[10] T. Kalaydzhyan, "Gravitational mass of relativistic matter and antimatter," *Physics Letters B*, vol. 751, pp. 29–33, 2015.

[11] R. A. Ferrell, "The positronium fine structure," *Phys. Rev.*, vol. 84, pp. 858–859, Nov 1951.

[12] T. Fulton and P. C. Martin, "Radiative corrections in positronium," *Phys. Rev.*, vol. 93, pp. 903–904, Feb 1954.

[13] T. Fulton, "Corrections to the Balmer-energy differences in positronium," *Phys. Rev. A*, vol. 26, pp. 1794–1795, Sep 1982.

[14] S. N. Gupta, W. W. Repko, and C. J. Suchyta, “Muonium and positronium potentials,” *Phys. Rev. D*, vol. 40, pp. 4100–4104, Dec 1989.

[15] R. N. Fell, “Order α^4 lnα^{-1} f_{ryd} corrections to the n=1 and n=2 energy levels of positronium,” *Phys. Rev. Lett.*, vol. 68, pp. 25–28, Jan 1992.

[16] K. Pachucki and S. G. Karshenboim, “Complete results for positronium energy levels at order $m\alpha^6$,” *Phys. Rev. Lett.*, vol. 80, pp. 2101–2104, Mar 1998.

[17] K. Pachucki and S. G. Karshenboim, “Higher-order recoil corrections to energy levels of two-body systems,” *Phys. Rev. A*, vol. 60, pp. 2792–2798, Oct 1999.

[18] G. S. Adkins, M. Kim, C. Parsons, and R. N. Fell, “Three-photon-annihilation contributions to positronium energies at order $m\alpha^7$,” *Phys. Rev. Lett.*, vol. 115, p. 233401, Dec 2015.

[19] P. J. Mohr, D. B. Newell, and B. N. Taylor, “CODATA recommended values of the fundamental physical constants: 2014,” *Rev. Mod. Phys.*, vol. 88, p. 035009, Sep 2016.

[20] M. S. Fee, A. P. Chu, S. andMills, Jr., R. J. Chichester, D. M. Zuckerman, E. D. Shaw, and K. Danzmann, “Measurement of the positronium $1^3S_1 - 2^3S_1$ interval by continuous-wave two-photon excitation,” *Phys. Rev. A*, vol. 48, pp. 192–219, Jul 1993.

[21] C. G. Parthey, A. Matveev, J. Alnis, B. Bernhardt, A. Beyer, R. Holzwarth, A. Maistrou, R. Pohl, K. Predehl, T. Udem, T. Wilken, N. Kolachevsky, M. Abgrall, D. Rovera, C. Salomon, P. Laurent, and T. W. Hänsch, “Improved measurement of the hydrogen $1s - 2s$ transition frequency,” *Phys. Rev. Lett.*, vol. 107, p. 203001, Nov 2011.

[22] S. Lundeen and F. Pipkin, “Measurement of the lamb shift in hydrogen, n= 2,” *Phys. Rev. Letters*, vol. 46, no. 4, p. 232, 1981.

[23] R. Pohl, A. Antognini, F. Nez, F. D. Amaro, F. Biraben, J. M. R. Cardoso, D. S. Covita, A. Dax, S. Dhawan, L. M. P. Fernandes, A. Giesen, T. Graf, T. W. Hänsch, P. Indelicato, L. Julien, C. Kao, P. Knowles, E. Le Bigot, Y.-W. Liu, J. A. M. Lopes, L. Ludhova, C. M. B. Monteiro, F. Mulhauser, T. Nebel, P. Rabinowitz, J. M. F. Dos Santos, L. A. Schaller, K. Schuhmann, C. Schwob, D. Taqqu, J. F. C. Veloso, and F. Kottmann, “The size of the proton,” *Nature*, vol. 466, no. 7303, pp. 213–216, 2010.

[24] A. Beyer, L. Maisenbacher, A. Matveev, R. Pohl, K. Khabarova, A. Grinin, T. Lamour, D. C. Yost, T. W. Hänsch, N. Kolachevsky, and T. Udem, “The Rydberg constant and proton size from atomic hydrogen,” *Science*, vol. 358, no. 6359, pp. 79–85, 2017.

[25] D. W. Higinbotham, V. Lin, D. Meekins, B. Norum, B. Sawatzky, *et al.*, “Proton radius from electron scattering data,” *Phys. Rev. C*, vol. 93, no. 5, p. 055207, 2016.

[26] G. Lee, J. R. Arrington, and R. J. Hill, “Extraction of the proton radius from electron-proton scattering data,” *Phys. Rev. D*, vol. 92, p. 013013, Jul 2015.

[27] M. Horbatsch and E. A. Hessels, "Evaluation of the strength of electron-proton scattering data for determining the proton charge radius," *Phys. Rev. C*, vol. 93, p. 015204, Jan 2016.

[28] A. P. Mills, Jr. and E. M. Gullikson, "Solid neon moderator for producing slow positrons," *App. Phys. Lett.*, vol. 49, no. 17, pp. 1121–1123, 1986.

[29] R. Khatri, M. Charlton, P. Sferlazzo, K. G. Lynn, A. P. Mills, Jr., and L. O. Roellig, "Improvement of rare-gas solid moderators by using conical geometry," *App. Phys. Lett.*, vol. 57, no. 22, pp. 2374–2376, 1990.

[30] C. M. Surko, M. Leventhal, and A. Passner, "Positron plasma in the laboratory," *Phys. Rev. Lett.*, vol. 62, pp. 901–904, Feb 1989.

[31] R. G. Greaves and C. M. Surko, "Positron trapping and the creation of high-quality trap-based positron beams," *Nucl. Instr. Meth. B*, vol. 192, no. 1, pp. 90 – 96, 2002.

[32] C. M. Surko and R. G. Greaves, "Emerging science and technology of antimatter plasmas and trap-based beams," *Physics of Plasmas*, vol. 11, no. 5, pp. 2333–2348, 2004.

[33] J. R. Danielson, D. H. E. Dubin, R. G. Greaves, and C. M. Surko, "Plasma and trap-based techniques for science with positrons," *Rev. Mod. Phys.*, vol. 87, pp. 247–306, Mar 2015.

[34] T. J. Murphy and C. M. Surko, "Positron trapping in an electrostatic well by inelastic collisions with nitrogen molecules," *Phys. Rev. A*, vol. 46, pp. 5696–5705, Nov 1992.

[35] R. G. Greaves and C. M. Surko, "Inward transport and compression of a positron plasma by a rotating electric field," *Phys. Rev. Lett.*, vol. 85, pp. 1883–1886, Aug 2000.

[36] R. G. Greaves and J. M. Moxom, "Compression of trapped positrons in a single particle regime by a rotating electric field," *Phys. Plasmas*, vol. 15, no. 7, p. 072304, 2008.

[37] M. R. Natisin, J. R. Danielson, and C. M. Surko, "Positron cooling by vibrational and rotational excitation of molecular gases," *J. Phys. B: At. Mol. Opt.*, vol. 47, no. 22, p. 225209, 2014.

[38] P. J. Schultz and K. G. Lynn, "Interaction of positron beams with surfaces, thin films, and interfaces," *Rev. Mod. Phys.*, vol. 60, pp. 701–779, Jul 1988.

[39] M. J. Puska and R. M. Nieminen, "Theory of positrons in solids and on solid surfaces," *Rev. Mod. Phys.*, vol. 66, pp. 841–897, Jul 1994.

[40] K. F. Canter, A. P. Mills, Jr., and S. Berko, "Efficient positronium formation by slow positrons incident on solid targets," *Phys. Rev. Lett.*, vol. 33, pp. 7–10, Jul 1974.

[41] A. P. Mills, Jr., "Positronium formation at surfaces," *Phys. Rev. Lett.*, vol. 41, pp. 1828–1831, Dec 1978.

[42] A. P. Mills, Jr. and L. Pfeiffer, “Desorption of surface positrons: A source of free positronium at thermal velocities,” *Phys. Rev. Lett.*, vol. 43, pp. 1961–1964, Dec 1979.

[43] D. B. Cassidy, T. H. Hisakado, H. W. K. Tom, and A. P. Mills, Jr., “Positronium formation via excitonlike states on Si and Ge surfaces,” *Phys. Rev. B*, vol. 84, p. 195312, Nov 2011.

[44] A. P. Mills, Jr., P. M. Platzman, and B. L. Brown, “Slow-positron emission from metal surfaces,” *Phys. Rev. Lett.*, vol. 41, pp. 1076–1079, Oct 1978.

[45] K. G. Lynn, “Observation of surface traps and vacancy trapping with slow positrons,” *Phys. Rev. Lett.*, vol. 43, pp. 391–394, Jul 1979.

[46] A. P. Mills, Jr., “Thermal activation measurement of positron binding energies at surfaces,” *Solid State. Commun.*, vol. 31, no. 9, pp. 623 – 626, 1979.

[47] A. P. Mills, Jr., L. Pfeiffer, and P. M. Platzman, “Positronium velocity spectroscopy of the electronic density of states at a metal surface,” *Phys. Rev. Lett.*, vol. 51, pp. 1085–1088, Sep 1983.

[48] D. J. Day, M. Charlton, and G. Laricchia, “On the formation of excited state positronium in vacuum by positron impact on untreated surfaces,” *J. Phys. B: At. Mol. Opt.*, vol. 34, no. 18, p. 3617, 2001.

[49] A. P. Mills, Jr., E. D. Shaw, M. Leventhal, R. J. Chichester, and D. M. Zuckerman, “Thermal desorption of cold positronium from oxygen-treated al (111) surfaces,” *Phys. Rev. B*, vol. 44, no. 11, p. 5791, 1991.

[50] D. B. Cassidy, T. H. Hisakado, V. E. Meligne, H. W. K. Tom, and A. P. Mills, Jr., “Delayed emission of cold positronium from mesoporous materials,” *Phys. Rev. A*, vol. 82, p. 052511, Nov 2010.

[51] A. P. Mills, Jr., E. D. Shaw, M. Leventhal, P. M. Platzman, R. J. Chichester, D. M. Zuckerman, T. Martin, R. Bruinsma, and R. R. Lee, “Evidence for quantum sticking of slow positronium,” *Phys. Rev. Lett.*, vol. 66, pp. 735–738, Feb 1991.

[52] D. B. Cassidy, P. Crivelli, T. H. Hisakado, L. Liszkay, V. E. Meligne, P. Perez, H. W. K. Tom, and A. P. Mills, Jr., “Positronium cooling in porous silica measured via doppler spectroscopy,” *Phys. Rev. A*, vol. 81, no. 1, p. 012715, 2010.

[53] A. C. L. Jones, T. H. Hisakado, H. J. Goldman, H. W. K. Tom, A. P. Mills, Jr., and D. B. Cassidy, “Doppler-corrected Balmer spectroscopy of Rydberg positronium,” *Phys. Rev. A*, vol. 90, p. 012503, Jul 2014.

[54] A. C. L. Jones, T. H. Hisakado, H. J. Goldman, H. W. K. Tom, and A. P. Mills, Jr., “Polarization dependence of n = 2 positronium transition rates to Stark-split n = 30 levels via crossed-beam spectroscopy,” *J. Phys. B: At. Mol. Opt.*, vol. 49, no. 6, p. 064006, 2016.

[55] R. J. Damburg and V. V. Kolosov, "Theoretical studies of hydrogen Rydberg atoms in electric fields," in *Rydberg States of Atoms and Molecules* (R. Stebbings and F. Dunning, eds.), Cambridge University Press, 1983.

[56] S. D. Hogan, "Calculated photoexcitation spectra of positronium Rydberg states," *Phys. Rev. A*, vol. 87, p. 063423, Jun 2013.

[57] A. I. Alekseev, "Two-photon annihilation of positronium in the p-state," *Sov. Phys. JETP*, vol. 7, p. 826, 1958.

[58] A. I. Alekseev, "Three-photon annihilation of positronium in the p-state," *Sov. Phys. JETP*, vol. 9, p. 1312, 1959.

[59] A. Deller, A. M. Alonso, B. S. Cooper, S. D. Hogan, and D. B. Cassidy, "Measurement of Rydberg positronium fluorescence lifetimes," *Phys. Rev. A*, vol. 93, p. 062513, Jun 2016.

[60] A. Siegman, *Lasers.* University Science Books, 1986.

[61] C. J. Hood, H. J. Kimble, and J. Ye, "Characterization of high-finesse mirrors: Loss, phase shifts, and mode structure in an optical cavity," *Phys. Rev. A*, vol. 64, p. 033804, Aug 2001.

[62] R. W. P. Drever, J. L. Hall, F. V. Kowalski, J. Hough, G. M. Ford, A. J. Munley, and H. Ward, "Laser phase and frequency stabilization using an optical resonator," *Appl. Phys. B*, vol. 31, pp. 97–105, Jun 1983.

[63] E. D. Black, "An introduction to Pound-Drever-Hall laser frequency stabilization," *Am. J. Phys.*, vol. 69, no. 1, pp. 79–87, 2001.

[64] M. Bass, C. DeCusatis, J. Enoch, V. Lakshminarayanan, G. Li, C. MacDonald, V. Mahajan, and E. Van Stryland, *Handbook of Optics, Third Edition Volume II: Design, Fabrication and Testing, Sources and Detectors, Radiometry and Photometry.* No. 2 in Handbook of Optics, McGraw-Hill Education, 2009.

[65] M. J. Martin and J. Ye, "High-precision laser stabilization via optical cavities," in *Optical Coatings and Thermal Noise in Precision Measurement* (G. Harry, T. Bodiya, and R. DeSalvo, eds.), Cambridge University Press, 2012.

[66] A. Yariv, "Quantum electronics, 3rd," *Edn.(John WieLy & Sons, New York, 1988) p*, vol. 389, 1989.

[67] L. Vasilenko, V. Chebotaev, and A. Shishaev, "Line shape of two-photon absorption in a standing-wave field in a gas," *ZhETF Pisma Redaktsiiu*, vol. 12, p. 161, 1970.

[68] W. Demtröder, *Laser Spectroscopy 2: Experimental Techniques.* Springer Berlin Heidelberg, 2015.

[69] A. P. Mills, Jr., E. D. Shaw, R. J. Chichester, and D. M. Zuckerman, "Positronium thermalization in SiO_2 powder," *Phys. Rev. B*, vol. 40, pp. 2045–2052, Aug 1989.

[70] M. Bruvelis, J. Ulmanis, N. N. Bezuglov, K. Miculis, C. Andreeva, B. Mahrov, D. Tretyakov, and A. Ekers, “Analytical model of transit time broadening for two-photon excitation in a three-level ladder and its experimental validation,” *Phys. Rev. A*, vol. 86, p. 012501, Jul 2012.

[71] A. C. L. Jones, A. M. Piñeiro, E. E. Roeder, H. J. Rutbeck-Goldman, H. W. K. Tom, and A. P. Mills, Jr., “Large-area field-ionization detector for the study of Rydberg atoms,” *Rev. Sci. Instrum.*, vol. 87, no. 11, p. 113307, 2016.

[72] A. C. L. Jones, J. Moxom, G. G. Cecchini, M. Fuentes-Garcia, E. Membreno, E. E. Roeder, and A. P. Mills, Jr., “A resistive-anode based position-sensitive Rydberg atom detector.” Manuscript in preparation, 2018.

[73] J. L. Wiza, “Microchannel plate detectors,” *Nucl. Instrum. Methods*, vol. 162, no. 1-3, pp. 587–601, 1979.

[74] J. Moore, C. Davis, M. Coplan, and S. Greer, *Building Scientific Apparatus*. Building Scientific Apparatus, Cambridge University Press, 2009.

[75] M. Lampton and C. W. Carlson, “Low-distortion resistive anodes for two-dimensional position-sensitive MCP systems,” *Rev. Sci. Instrum.*, vol. 50, no. 9, pp. 1093–1097, 1979.

[76] A. C. L. Jones, J. Moxom, H. J. Rutbeck-Goldman, K. A. Osorno, G. G. Cecchini, M. Fuentes-Garcia, R. G. Greaves, D. J. Adams, H. W. K. Tom, A. P. Mills, Jr., and M. Leventhal, “Focusing of a Rydberg positronium beam with an ellipsoidal electrostatic mirror,” *Phys. Rev. Lett.*, vol. 119, p. 053201, Aug 2017.

[77] D. W. Allan, “Statistics of atomic frequency standards,” *Proceedings of the IEEE*, vol. 54, pp. 221–230, Feb 1966.

[78] EndRun Technologies, *Meridian II Precision TimeBase User Manual*, usm3043-0000-000 revision 6 ed., August 2017.

[79] J. Cariou and P. Luc, *Atlas du Spectre dAbsorption de la Molecule Tellure*. Laboratoire Aime-Cotton, CNRS II, Orsay, France, 1980.

[80] G. P. Barwood, W. R. C. Rowley, P. Gill, J. L. Flowers, and B. W. Petley, “Interferometric measurements of ^{130}Te$_2$ reference frequencies for 1S-2S transitions in hydrogenlike atoms,” *Phys. Rev. A*, vol. 43, pp. 4783–4790, May 1991.

[81] R. E. Machol and E. F. Westrum, “Vapor pressure of liquid tellurium,” *J. Am. Chem. Soc.*, vol. 80, no. 12, pp. 2950–2952, 1958.

[82] J. D. Gillaspy and C. J. Sansonetti, “Absolute wavelength determinations in molecular tellurium: new reference lines for precision laser spectroscopy,” *J. Opt. Soc. Am. B*, vol. 8, pp. 2414–2419, Dec 1991.

[83] D. H. McIntyre, W. M. Fairbank, S. A. Lee, T. W. Hänsch, and E. Riis, "Interferometric frequency measurement of $^{130}\mathrm{Te}_2$ reference transitions at 486 nm," *Phys. Rev. A*, vol. 41, pp. 4632–4635, May 1990.